Editors' Suggestion

Light nuclei with semilocal momentum-space regularized chiral interactions up to third order

P. Maris,[1,*] E. Epelbaum,[2] R. J. Furnstahl,[3] J. Golak,[4] K. Hebeler,[5,6] T. Hüther,[5] H. Kamada,[7] H. Krebs,[2] Ulf-G. Meißner,[8,9,10] J. A. Melendez,[3] A. Nogga,[9] P. Reinert,[2] R. Roth,[5] R. Skibiński,[4] V. Soloviov,[4] K. Topolnicki,[4] J. P. Vary,[1] Yu. Volkotrub,[4] H. Witała,[4] and T. Wolfgruber[5]
(LENPIC Collaboration)
[1]*Department of Physics and Astronomy, Iowa State University, Ames, Iowa 50011, USA*
[2]*Ruhr-Universität Bochum, Fakultät für Physik und Astronomie, Institut für Theoretische Physik II, D-44780 Bochum, Germany*
[3]*Department of Physics, The Ohio State University, Columbus, Ohio 43210, USA*
[4]*M. Smoluchowski Institute of Physics, Jagiellonian University, PL-30348 Kraków, Poland*
[5]*Institut für Kernphysik, Technische Universität Darmstadt, 64289 Darmstadt, Germany*
[6]*ExtreMe Matter Institute EMMI, GSI Helmholtzzentrum für Schwerionenforschung GmbH, 64291 Darmstadt, Germany*
[7]*Department of Physics, Faculty of Engineering, Kyushu Institute of Technology, Kitakyushu 804-8550, Japan*
[8]*Helmholtz-Institut für Strahlen- und Kernphysik and Bethe Center for Theoretical Physics, Universität Bonn, D-53115 Bonn, Germany*
[9]*Institut für Kernphysik, Institute for Advanced Simulation and Jülich Center for Hadron Physics, Forschungszentrum Jülich, D-52425 Jülich, Germany*
[10]*Tbilisi State University, 0186 Tbilisi, Georgia*

(Received 2 January 2021; accepted 13 April 2021; published 5 May 2021)

We present a systematic investigation of few-nucleon systems and light nuclei using the current Low Energy Nuclear Physics International Collaboration interactions comprising semilocal momentum-space regularized two- and three-nucleon forces up to third chiral order (N^2LO). Following our earlier study utilizing the coordinate-space regularized interactions, the two low-energy constants entering the three-body force are determined from the triton binding energy and the differential cross-section minimum in elastic nucleon-deuteron scattering. Predictions are made for selected observables in elastic nucleon-deuteron scattering and in the deuteron breakup reactions, for properties of the $A = 3$ and $A = 4$ nuclei, and for spectra of p-shell nuclei up to $A = 16$. A comprehensive error analysis is performed including an estimation of correlated truncation uncertainties for nuclear spectra. The obtained predictions are generally found to agree with experimental data within errors. Similarly to the coordinate-space regularized chiral interactions at the same order, a systematic overbinding of heavier nuclei is observed, which sets in for $A \sim 10$ and increases with A.

DOI: 10.1103/PhysRevC.103.054001

I. INTRODUCTION

A reliable quantitative first-principles description of nuclear structure and reactions with quantified uncertainties remains one of the main challenges in computational nuclear physics. Presently, the most promising approach to reach this ambitious goal comprises a combination of chiral effective field theory (EFT) to describe nuclear interactions in harmony with the symmetries (and their breaking pattern) of QCD with *ab initio* few-body methods to tackle the quantum mechanical A-body problem. Remarkable progress has been achieved in recent years in both lines of research, see Refs. [1–13] for a selection of review articles on these topics. At least for not-too-heavy nuclei, the accuracy of theoretical predictions is, in most cases, limited by the uncertainties of the nuclear interactions.

To address this challenge, the Low Energy Nuclear Physics International Collaboration aims at developing accurate and precise two- and three-nucleon forces (3NF) by pushing the EFT expansion to high chiral orders and using these interactions to solve the structure and reactions of light nuclei. In Refs. [14–16], we have already explored selected nucleon-deuteron (Nd) scattering observables and the structure of light- and medium-mass nuclei up to $A = 48$ using the new generation of the chiral EFT nucleon-nucleon potentials from Refs. [17,18] up through fifth chiral order (N^4LO). The essential new feature of these interactions as compared to the older potentials of Refs. [19,20] and the new potentials developed by Entem *et al.* [21] is the usage of a *local* regulator for pion-exchange contributions, which allowed us to substantially reduce finite-cutoff artifacts. These novel interactions have also been successfully tested in selected electroweak reactions with two and three nucleons [22,23]. While these exploratory studies employed NN interactions only and thus should be regarded as incomplete starting from next-to-next-to-leading order (N^2LO), the chiral order at which the 3NF starts to contribute, they brought important new insights into the convergence pattern of the chiral expansion. In particular, the resulting discrepancies between theory and experimental

*pmaris@iastate.edu

data were found to be in agreement with the expected size of the missing 3NF contributions according to the Weinberg power counting [14].

The expressions for the 3NF have been worked out completely up to fourth chiral order (N^3LO) using dimensional regularization to deal with divergent loop integrals [24–26]; see also Refs. [27,28] for selected results at N^4LO. A numerical implementation of the 3NF in the Faddeev and Yakubovsky equations requires its partial-wave decomposition, which can, in principle, be carried out in a brute-force way by numerically performing the relevant angular integrations [29,30]. However, a coordinate-space regulator for the long-range components of the 3NF, in line with the NN potentials of Refs. [17,18], was found to lead to numerical instabilities when performing its partial-wave decomposition. While this issue has been finally solved for the 3NF at tree level (i.e., at N^2LO) [31], an extension of these studies to higher chiral orders is a nontrivial task that would require further substantial efforts.

These findings motivated the development of the semilocal momentum-space regularized (SMS) NN potentials in Ref. [32], where both the short-range and long-range contributions to the interaction are regularized in momentum space. The other important differences to the semilocal coordinate-space regularized (SCS) potentials of Refs. [17,18] comprise the removal of three redundant short-range operators at N^3LO and the usage of the most up-to-date values of the pion-nucleon low-energy constants (LECs) from the Roy-Steiner equation analysis of Ref. [33,34]. Moreover, contrary to our earlier studies [17,18] that relied on the Nijmegen partial-wave analysis [35], the LECs accompanying the contact interactions have been determined directly from the mutually consistent neutron-proton and proton-proton scattering data of the 2013 Granada database [36]. At the highest considered order N^4LO^+, where the "+" signifies the inclusion of four sixth-order contact interactions in F-waves in order to describe certain very precise proton-proton scattering data,[1] the NN potentials of Ref. [32] allow for an outstanding description of the NN scattering data from the 2013 Granada database below pion-production threshold. In Ref. [37], these interactions have been extended by taking into account isospin-breaking contributions up to N^4LO. These are currently the most precise chiral NN interactions on the market, which for the intermediate cutoff value of $\Lambda = 450$ MeV even qualify to be regarded as a partial-wave analysis up to $E_{\rm lab} = 300$ MeV. These novel chiral EFT NN potentials have already been successfully applied to Nd scattering [38,39] and to the ^{2}H and ^{3}He electroweak disintegration processes [40]. They were also used in the recent high-accuracy calculation of the electromagnetic form factors of the deuteron [41,42] and allowed, in particular, the prediction of the structure radius (quadrupole moment) of the deuteron with remarkable accuracy at the permille (percentage) level.

In this paper we present, for the first time, results for p-shell nuclei based on the SMS NN potentials of Ref. [32] and also include the dominant 3NF at N^2LO using the same regulator as employed in the two-body interactions. We employ the same convention for the long-range 3NF as used in the NN interactions by subtracting the locally regularized short-range terms to ensure that the corresponding regularized three-nucleon potentials vanish at the origin. Finally, we address the important issue of estimating truncation errors for strongly correlated observables such as the excitation energy spectra, see Ref. [16] for a discussion.

Our paper is organized as follows. In Sec. II we provide the expressions for the regularized 3NF and describe the determination of the LECs c_D and c_E from selected experimental data in the three-nucleon system. Our predictions for selected Nd scattering and breakup observables up to N^2LO are summarized in Sec. III. Next, Secs. IV and V are focused on the properties of light nuclei with $A = 3, 4$ and on the energy spectra of p-shell nuclei up to $A = 16$, respectively. In Sec. VI we perform an uncertainty analysis of the obtained predictions for the energy spectra of light nuclei using a correlated error Bayesian model. This allows us, for the first time, to reliably estimate the truncation errors of our predictions for the excitation energies. Finally, the most important results of this study are summarized in Sec. VII.

II. DETERMINATION OF c_D AND c_E

Throughout this work, we employ the N^2LO three-nucleon force (3NF) regularized in momentum space in the same way as the SMS two-nucleon interaction of Ref. [32], namely

$$
\begin{aligned}
V_\Lambda^{\rm 3N} = {} & \frac{g_A^2}{8F_\pi^4}\, e^{-\frac{\vec{q}_1^{\,2}+M_\pi^2}{\Lambda^2}}\, e^{-\frac{\vec{q}_3^{\,2}+M_\pi^2}{\Lambda^2}} \left\{ \frac{\vec{\sigma}_1\cdot\vec{q}_1\;\vec{\sigma}_3\cdot\vec{q}_3}{\left(\vec{q}_1^{\,2}+M_\pi^2\right)\left(\vec{q}_3^{\,2}+M_\pi^2\right)} \right. \\
& \times\left[T_{13}\left(2c_3\,\vec{q}_1\cdot\vec{q}_3 - 4c_1 M_\pi^2\right) + c_4 T_{132}\,\vec{q}_1\times\vec{q}_3\cdot\vec{\sigma}_2\right] \\
& + C\,\frac{\vec{\sigma}_1\cdot\vec{q}_1}{\vec{q}_1^{\,2}+M_\pi^2}\left(2c_3\,T_{13}\,\vec{\sigma}_3\cdot\vec{q}_1 + c_4 T_{132}\,\vec{q}_1\times\vec{\sigma}_3\cdot\vec{\sigma}_2\right) \\
& + C\,\frac{\vec{\sigma}_3\cdot\vec{q}_3}{\vec{q}_3^{\,2}+M_\pi^2}\left(2c_3\,T_{13}\,\vec{\sigma}_1\cdot\vec{q}_3 + c_4 T_{132}\,\vec{\sigma}_1\times\vec{q}_3\cdot\vec{\sigma}_2\right) \\
& \left. + C^2\left(2c_3\,T_{13}\,\vec{\sigma}_1\cdot\vec{\sigma}_3 + c_4 T_{132}\,\vec{\sigma}_1\times\vec{\sigma}_3\cdot\vec{\sigma}_2\right)\right\} \\
& - \frac{g_A\,D}{8F_\pi^2}\,T_{13}\,e^{-\frac{\vec{p}_{12}^{\,2}+\vec{p}_{12}^{\,\prime 2}}{\Lambda^2}}\,e^{-\frac{\vec{q}_3^{\,2}+M_\pi^2}{\Lambda^2}}\left[\frac{\vec{\sigma}_3\cdot\vec{q}_3}{\vec{q}_3^{\,2}+M_\pi^2}\,\vec{\sigma}_1\cdot\vec{q}_3\right. \\
& \left. + C\,\vec{\sigma}_1\cdot\vec{\sigma}_3\right] + \frac{1}{2}E\;T_{12}\,e^{-\frac{\vec{p}_{12}^{\,2}+\vec{p}_{12}^{\,\prime 2}}{\Lambda^2}}\,e^{-\frac{3\vec{k}_3^{\,2}+3\vec{k}_3^{\,\prime 2}}{4\Lambda^2}} \\
& + 5\ \text{permutations}, \qquad (1)
\end{aligned}
$$

where $\vec{q}_i = \vec{p}_i\,' - \vec{p}_i$ is the momentum transfer of nucleon i with $\vec{p}_i\,'$ and $\vec{p}_i$ referring to the corresponding final and initial momenta, respectively, $T_{ij} \equiv \boldsymbol{\tau}_i\cdot\boldsymbol{\tau}_j$, $T_{ijk} \equiv \boldsymbol{\tau}_i\times\boldsymbol{\tau}_j\cdot\boldsymbol{\tau}_k$, and $\vec{\sigma}_i$ ($\boldsymbol{\tau}_i$) are the Pauli spin (isospin) matrices. We have also introduced the Jacobi momenta $\vec{p}_{12} = (\vec{p}_1 - \vec{p}_2)/2$ and $\vec{k}_3 = 2(\vec{p}_3 - (\vec{p}_1 + \vec{p}_2)/2)/3$ in the initial state and $\vec{p}\,'_{12} = (\vec{p}\,'_1 - \vec{p}\,'_2)/2$ and $\vec{k}\,'_3 = 2(\vec{p}\,'_3 - (\vec{p}\,'_1 + \vec{p}\,'_2)/2)/3$ in the final state. Further, g_A, F_π, and M_π refer to the nucleon axial vector coupling, pion decay constant, and pion mass, respectively, while the

[1]The same short-range operators are also included in the N^4LO version of the potentials of Ref. [21].

subtraction constant C is given by [32]

$$C = -\frac{\Lambda(\Lambda^2 - 2M_\pi^2) + 2\sqrt{\pi} M_\pi^3 e^{\frac{M_\pi^2}{\Lambda^2}} \mathrm{erfc}\left(\frac{M_\pi}{\Lambda}\right)}{3\Lambda^3}, \quad (2)$$

where $\mathrm{erfc}(x)$ is the complementary error function

$$\mathrm{erfc}(x) = \frac{2}{\sqrt{\pi}} \int_x^\infty dt\, e^{-t^2}. \quad (3)$$

Finally, for the LECs D and E, we employ the standard parametrization in terms of dimensionless constants c_D and c_E via $D = c_D/(F_\pi^2 \Lambda_\chi)$ and $E = c_E/(F_\pi^4 \Lambda_\chi)$ with $\Lambda_\chi = 700$ MeV.

The subtraction terms proportional to C in Eq. (1) correspond to the *convention* employed in Ref. [32]. It ensures, for example, that the locally regularized two-pion exchange 3NF in the curly brackets, Fourier transformed to coordinate space, vanishes at the origin (i.e., for $\vec{r}_1 - \vec{r}_2 \to 0$ or $\vec{r}_3 - \vec{r}_2 \to 0$) in order to minimize the admixture of short-range components. The applied regularization scheme, therefore, utilizes a local (nonlocal) regulator for long-range (short-range) components of the 3NF.

Partial-wave decomposition of the 3NF is accomplished numerically in momentum space in the usual way as described in detail in Refs. [29,30,43]. Moreover, we have benchmarked the momentum-space results by independently carrying out the partial-wave decomposition in coordinate space. This way we have also explicitly verified that the subtracted long-range potentials vanish at the origin as required by our convention.

We are now in the position to specify the values of the various LECs. For the pion-nucleon constants c_i, we employ the values from matching chiral perturbation theory at next-to-leading order (NLO) in the NN-counting scheme to the solutions of the Roy-Steiner equations for pion-nucleon scattering [33,34]:

$$\begin{aligned} c_1 &= -0.74\ \mathrm{GeV}^{-1}, \\ c_3 &= -3.61\ \mathrm{GeV}^{-1}, \\ c_4 &= 2.44\ \mathrm{GeV}^{-1}. \end{aligned} \quad (4)$$

The same values are used in the SMS NN potentials of Ref. [32] at next-to-next-to-leading order ($\mathrm{N^2LO}$).

To determine the values of the LECs c_D, c_E, we require, following our previous studies [31,44–46], that the ^{3}H binding energy is reproduced exactly. This constraint yields c_E as a function of the LEC c_D for every value of the cutoff Λ. In Fig. 1, we show the resulting c_D–c_E correlations for the cutoff values $\Lambda = 450$ and 500 MeV. As one may expect, the behavior is qualitatively similar to the one found using the SCS interactions in Ref. [31]. In particular, the larger momentum-space cutoff leads to a larger-in-magnitude negative slope of the function $c_E(c_D)$, exhibiting more nonlinear behavior.

Motivated by our findings in Ref. [31], the determination of the remaining LEC c_D is carried out by fitting the experimental data of Ref. [47] for the differential cross-section minimum at the nucleon beam energy of $E_N = 70$ MeV. Specifically, the values of c_D are determined from a least-squares fit of 12 cross-section data points in the angular range of $\theta_{\mathrm{c.m.}} \in [107.0^\circ, 140.4^\circ]$ with the Coulomb force contribution subtracted [48], and the statistical and systematic errors added in quadrature. This leads to the following central values:

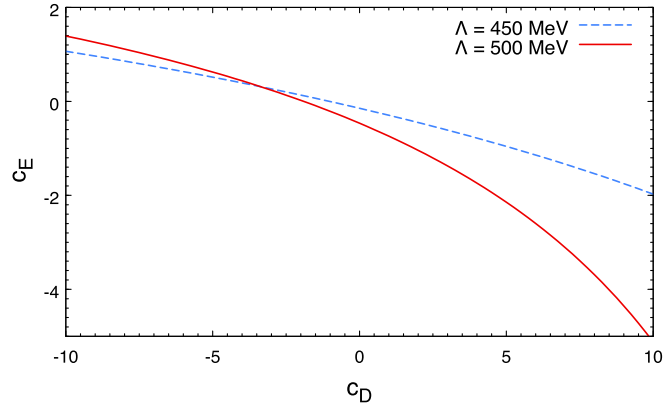

FIG. 1. Correlation between the LECs c_D and c_E induced by the requirement that the ^{3}H binding energy be reproduced for the cutoff choices of $\Lambda = 450$ MeV (blue dashed line) and $\Lambda = 500$ MeV (red solid line).

$$\begin{aligned} c_D &= \ \ 2.485, \quad c_E = -0.528 \quad \text{for} \ \ \Lambda = 450\ \mathrm{MeV}, \\ c_D &= -1.626, \quad c_E = -0.063 \quad \text{for} \ \ \Lambda = 500\ \mathrm{MeV}. \end{aligned} \quad (5)$$

The determination of uncertainties in the values of c_D, c_E and their propagation will be considered in a separate publication.

III. NUCLEON-DEUTERON SCATTERING

We are now in the position to show selected results for Nd scattering observables. For a description of our formalism for solving the Faddeev-type integral equations, see Ref. [49]. To estimate the truncation errors at $\mathrm{N^2LO}$, we employ the Bayesian model $\bar{C}^{650}_{0.5-10}$ introduced in Ref. [38] based on the ideas of Refs. [17,50–52]. Specifically, for a three-nucleon scattering observable $X(E_N)$, we consider the chiral EFT expansion up to $\mathrm{N^2LO}$,

$$\begin{aligned} X &= X^{(0)} + \Delta X^{(2)} + \Delta X^{(3)} + \ldots \\ &=: X_{\mathrm{ref}}(c_0 + c_2 Q^2 + c_3 Q^3 + \ldots), \end{aligned} \quad (6)$$

where $\Delta X^{(2)} := X^{(2)} - X^{(0)}$ and $\Delta X^{(3)} := X^{(3)} - X^{(2)}$, Q is the expansion parameter, the superscripts denote the chiral order Q^n, the ellipses refer to terms beyond $\mathrm{N^2LO}$, the quantity X_{ref} sets the overall scale and c_i are the corresponding dimensionless coefficients.[2] The reference scale X_{ref} is chosen using the information from all three available chiral orders as described in Ref. [38]. Assuming that all dimensionless coefficients c_i are normally distributed with the Gaussian prior

$$\mathrm{pr}(c_i|\bar{c}) = \frac{1}{\sqrt{2\pi}\,\bar{c}}\, e^{-c_i^2/(2\bar{c}^2)}, \quad (7)$$

and performing marginalization over the first $h = 10$ neglected orders for a uniform distribution of the

[2]Here and in Sec. VI we use the conventional notation c_i for the Bayesian expansion coefficients, not to be confused with the pion-nucleon LECs c_1, c_3, and c_4 in Sec. II.

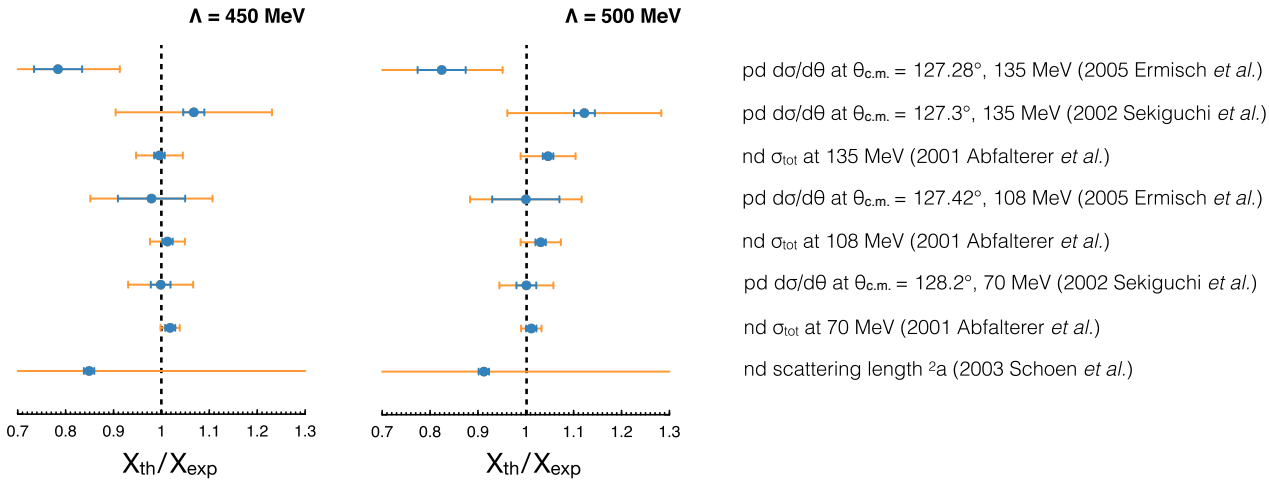

FIG. 2. Predictions for various Nd scattering observables based on the c_D and c_E values given in Eq. (5). For every considered observable X, a solid dot corresponds to the ratio of its calculated value $X_{\rm th}$ at N^{2}LO to the corresponding experimental value $X_{\rm exp}$. The smaller (blue) error bars correspond to the experimental relative uncertainty $\delta X_{\rm exp}/X_{\rm exp}$, where $\delta X_{\rm exp}$ includes both the statistical and systematic errors added in quadrature. The larger (orange) error bars also take into account the estimated 68% DoB truncation error $\delta X_{\rm th}$ and correspond to $\sqrt{\delta X_{\rm exp}^2 + \delta X_{\rm th}^2}/X_{\rm exp}$. For the Nd doublet scattering length ^2a, this relative error amounts to ± 0.71 (± 0.88) for $\Lambda = 450$ MeV ($\Lambda = 500$ MeV). Experimental data are from Ref. [53], Ref. [54], Ref. [47], and Ref. [55].

hyperparameter $\bar{c}$ in the range of $\bar{c} \in [0.5, 10]$, one obtains an analytical expression for the posterior probability distribution $\mathrm{pr}_h(\Delta|\{c_i\})$ for the dimensionless residual $\Delta_3 := c_4 Q^4 + \ldots + c_{3+h} Q^{3+h}$ to take a value Δ given the known coefficients c_0, c_2, and c_3, see Refs. [38,51] for details. This expression can be used to obtain truncation errors corresponding to any given degree-of-belief (DoB) interval. Following Ref. [38], the expansion parameter Q is defined according to

$$Q = \max\left(\frac{p}{\Lambda_b}, \frac{M_\pi^{\rm eff}}{\Lambda_b}\right), \tag{8}$$

with $M_\pi^{\rm eff} = 200$ MeV and the breakdown scale $\Lambda_b = 650$ MeV [52]. The momentum p is related to the laboratory energy E_N of a given 3N scattering observable via [38]

$$p = \sqrt{\frac{2}{3} m E_N} \tag{9}$$

with m denoting nucleon mass.

In our earlier paper describing results for the SCS interactions [31], the values of the LEC c_D have been determined from a combined fit to the Nd doublet scattering length ^2a as well as the total nd cross section and the pd differential cross-section data in the minimum region at the nucleon energies of $E_N = 70$ MeV, 108 MeV, and 135 MeV. While we have used only the differential cross-section data at the lowest energy of 70 MeV in the present work, we show in Fig. 2 that our c_D determination is indeed consistent with the mentioned observables. Note that for unnaturally small observables such as the Nd doublet scattering length ^2a, one needs to go to high order in the chiral expansion to achieve a small relative error. The experimental value is $^2a = (0.645 \pm 0.008)$ fm, whereas the estimated 68% DoB chiral truncation errors are 0.46 fm and 0.54 fm, corresponding to relative truncation errors of 0.71 and 0.88, at $\Lambda = 450$ and 500 MeV, respectively.

The only disagreement is observed for the differential cross-section data at $E_N = 135$ MeV measured at KVI [55], which also disagree with the data of Ref. [47] at the same energy, see the blue error bars in Fig. 2. While our results indicate a slight preference for the experimental data of Ref. [47], the relatively large truncation errors at N^{2}LO do not allow one to make a stronger conclusion at this stage.

In Fig. 3, we show our NLO and N^{2}LO predictions for selected observables in elastic Nd scattering at $E_N = 70$ MeV. Notice that the truncation errors are symmetric, and the actual results of our calculation lie in the middle of the corresponding error bands. At both NLO and N^{2}LO, the experimental data are, in most cases, reasonably well described by our calculations. We also compare our results to those of Ref. [38] based on the same NN interactions but using the unsubtracted version of the 3NF, as well as to our earlier results using the SCS two- [17] and three-nucleon forces from Ref. [31] at the regulator value $R = 0.9$ fm. It is reassuring to see that all shown N^{2}LO results agree with each other within errors.

We have also calculated selected breakup observables at $E_N = 65$ MeV, for which experimental data are available. In Fig. 4, we show the fivefold differential cross section and nucleon vector analyzing power A_y as functions of the kinematical locus variable S for selected configurations specified by the detection angles θ_1, θ_2, and ϕ_{12} in the laboratory system; see Ref. [49] for the definition of kinematical variables, which may serve as representative examples.

One observes a similar picture as for the considered elastic scattering observables. In particular, the experimental data are well reproduced, and our N^{2}LO results agree well with those obtained both using the SCS (NN+3NF) interactions and the SMS forces with unsubtracted 3NF. Furthermore, our N^{2}LO results for the differential cross sections in Fig. 4 agree well with the predictions based on the CD Bonn potential, see Fig. 6 of Ref. [58]. This should not come as a surprise

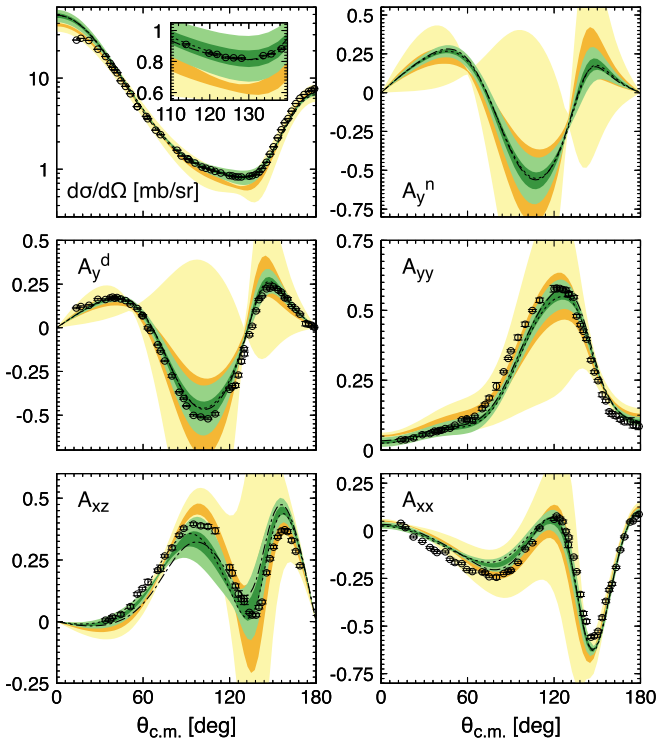

FIG. 3. Results for the differential cross section, nucleon, and deuteron analyzing powers A_y^n and A_y^d as well as deuteron tensor analyzing powers A_{yy}, A_{xz}, and A_{xx} in elastic nucleon-deuteron scattering at laboratory energy of $E_N = 70$ MeV at NLO (yellow bands) and N^{2}LO (green bands) for $\Lambda = 450$ MeV. Dotted lines show the N^{2}LO results based on the SMS NN forces from Ref. [32] accompanied with the *unsubtracted* [i.e., with $C(M_\pi) = 0$] 3NF from Ref. [38], while dashed-dotted lines are N^{2}LO predictions based on the SCS (NN+3NF) interactions from Ref. [31]. The light (dark) shaded bands indicate 95% (68%) DoB intervals using the Bayesian model $\bar{C}^{650}_{0.5-10}$. Open circles are proton-deuteron data from Ref. [47].

since 3NF effects appear to be fairly small for the considered cases. Notice, however, that relativistic corrections turn out to be non-negligible for the cross section in Figs. 4(d) and 4(e). In Ref. [58], they were found to decrease the predictions for the differential cross section around the maximum by almost 10%. In chiral EFT, relativistic corrections to the Nd scattering amplitude need to be taken into account starting from N^{3}LO. Their expected size is, therefore, in qualitative agreement with the estimated size of the neglected N^{3}LO contributions as reflected by the width of the green uncertainty bands. Finally, we have also calculated breakup configurations considered in Ref. [59], which feature more pronounced 3NF effects. In all considered cases (not shown here), we found similar results to the ones based on high-precision phenomenological NN potentials in combinations with the Urbana IX [60] and the updated Tucson-Melbourne [61] 3NF models.

IV. $A = 3$ AND 4 NUCLEI

With the interactions specified in the previous section, we now calculate the ground-state energies and excitation spectra up to the p shell. In this section, we focus on the $A = 3$ and $A = 4$ bound states, for which we solve Faddeev and Yakubovsky equations in momentum space as outlined in Ref. [16]. The addition of 3NFs has been discussed in Ref. [62].

For $A = 3$, we reach a numerical accuracy of 1 keV for the binding energy and the expectation values. For practical calculations, the number of partial-wave channels needs to be truncated. To reach the desired accuracy, we take into account all partial waves with two-body subsystem angular momentum less than or equal to 5. This includes a small admixture of total isospin $T = 3/2$ states in ^{3}H and ^{3}He. It has been shown in Ref. [63] that this is necessary to reach the same accuracy for the expectation values of the Hamiltonian.

In ^{3}He, additionally, the point Coulomb interaction has been included for the pp subsystem. For the numerical calculation in momentum space, the Coulomb force has been Fourier transformed using a cutoff at distances of 20 fm. It has been checked that larger distances do not contribute to the 3N binding energies.

Our results are summarized in Table I for LO, NLO, and N^{2}LO interactions. For N^{2}LO, we also give results for NN interactions only.

It can been seen that the binding energy $|E|$ based purely on NN interactions decreases for both cutoffs when the chiral order increases. At N^{2}LO, an attractive contribution of the 3NF increases the binding energy and brings it, by construction, in agreement with the experimental value of -8.482 MeV for ^{3}H [64]. For the calculation of the energies, we used an averaged proton and neutron mass of 938.918 MeV. The slight deviation of the expectation values $\langle H \rangle$ from the binding energy is due to the additional contribution $\langle T_{\rm CSB} \rangle$ resulting from employing physical proton and neutron masses. Due to the larger binding energy this effect is more pronounced at LO. The approximately ± 6 keV for ^{3}He and ^{3}H for NLO and N^{2}LO are in line with the results for phenomenological interactions [63]. Including this contribution, we find in LO, NLO, and N^{2}LO (including the 3NF) for $\Lambda = 500$ MeV a charge symmetry breaking (CSB) difference of the binding energies of 910, 764, and 755 keV comparable to the experimental value of 764 keV. Results for $\Lambda = 450$ MeV are very similar.

It is well known that the partial-wave convergence of Faddeev components for the 3N system is faster than the convergence of the wave functions. Therefore, it is advantageous to normalize the overlap of Faddeev components and wave functions [16]. Missing high partial waves then lead to a deviation of the norm $\langle \Psi | \Psi \rangle$ of the 3N system from one. The size of this effect is larger when higher orders of the interactions or 3NFs are employed, indicating that these interactions induce contributions to higher partial waves. In all cases, our truncation of the partial-wave basis provides more than 99.9% off the norm.

Table I also summarizes the S-, P-, and D-state probabilities. As usual, the contribution of the P-state is small. The D-state visibly contributes, where again the higher orders and especially 3NFs lead to an increasing D-state probability. This is in line with results based on different interactions [62].

Finally, we also give values for point-proton and neutron matter radii r_p and r_n. These have been obtained based on a

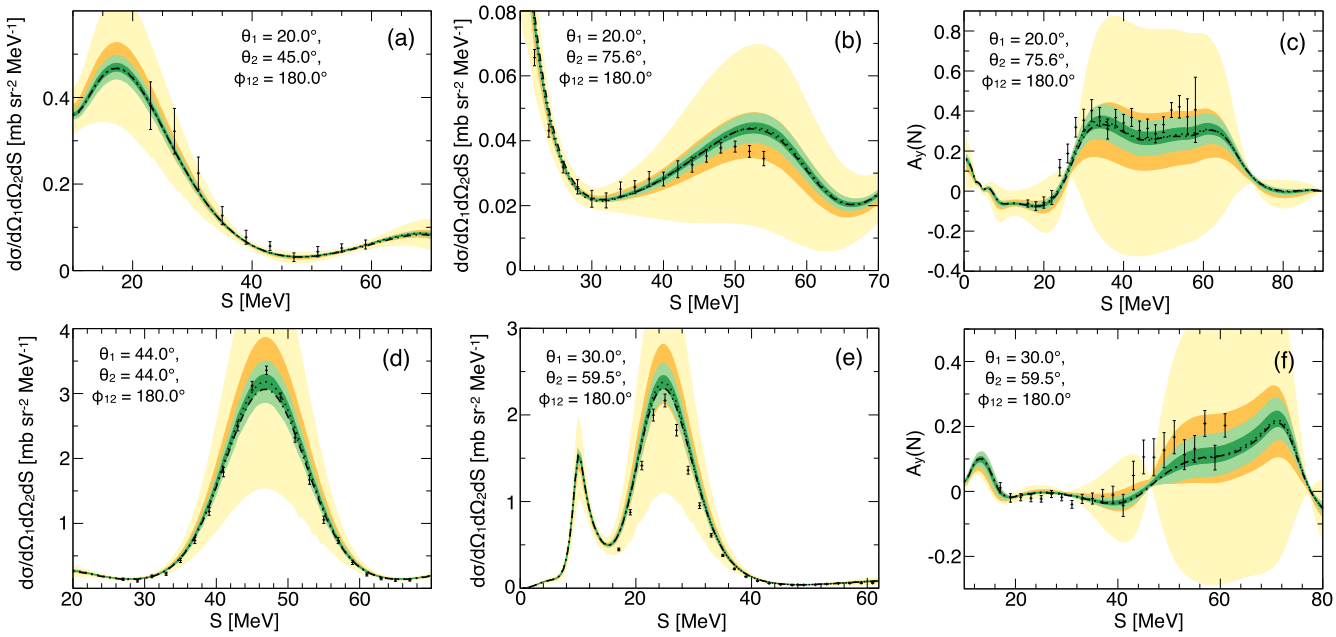

FIG. 4. Results for the differential cross section [left and center, (a), (b), (d), and (e)] and nucleon vector analyzing power A_y, [right, (c) and (f)], as functions of the kinematical locus variable S for the deuteron breakup reaction at laboratory energy of $E_N = 65$ MeV at NLO (yellow bands) and N^{2}LO (green bands) for $\Lambda = 450$ MeV. Proton-deuteron data for (a)–(c) are taken from Ref. [56] while those shown in (d)–(f) are from Ref. [57]. For remaining notation see Fig. 3.

Fourier transform of the wave functions. The observed pattern showing increasing (decreasing) values of the radii with the chiral order (when adding the 3NF) are qualitatively in line with the changes in binding energy. Note however that 3NFs break this correlation to some extent.

For $A = 4$, we solve the set of Yakubovsky equations. Since three orbital angular momenta contribute to the partial-wave expansion, we need to constrain at least two of them to end up with a finite number of partial waves. For the calculations done here, we again use the two-body subsystem angular momentum to less than or equal to 5. Additionally, we only use orbital angular momenta less than or equal to 6 and also constrain the sum of all orbital angular momenta to 10 or less. We also use isospin symmetry and therefore only take the by-far dominant isospin $T = 0$ channels into account. We checked that these constraints lead to an uncertainty of approximately 10 keV for the binding energies and 50 keV for the expectation values. Since we only take isospin $T = 0$

TABLE I. Summary of energies and wave-function properties for ^{3}H/^{3}He. See text for explanations. Energies and cutoffs are given in MeV except for $\langle T_{\rm CSB}\rangle$ which is given in keV. Radii are given in fm and the S-, P-, and D-state probabilities are given in %.

		Λ	E	$\langle H\rangle$	$\langle T\rangle$	$\langle V_{NN}\rangle$	$\langle V_{\rm 3NF}\rangle$	$\langle T_{\rm CSB}\rangle$	$\langle\Psi\|\Psi\rangle$	P(S)	P(P)	P(D)	r_p	r_n
^{3}H	LO	450	−12.22	−12.24	52.38	−64.61		−10.505	1.0000	96.25	0.019	3.73	1.250	1.319
	NLO		−8.515	−8.521	34.31	−42.82		−5.798	0.9999	94.79	0.028	5.19	1.556	1.702
	N^{2}LO (NN-only)		−8.143	−8.148	34.94	−43.08		−5.552	0.9998	93.28	0.044	6.68	1.595	1.752
	N^{2}LO+3NFs		−8.483	−8.489	36.13	−44.16	−0.459	−5.840	0.9995	92.54	0.077	7.38	1.576	1.725
^{3}H	LO	500	−12.52	−12.53	57.84	−70.36		−11.528	0.9999	94.96	0.036	5.01	1.224	1.286
	NLO		−8.325	−8.332	35.87	−44.19		−6.150	0.9998	94.29	0.032	5.68	1.575	1.725
	N^{2}LO (NN-only)		−7.920	−7.926	37.94	−45.86		−5.754	0.9996	92.06	0.059	7.89	1.625	1.787
	N^{2}LO+3NFs		−8.482	−8.488	40.27	−48.09	−0.660	−6.24	0.9992	91.39	0.109	8.50	1.581	1.731
^{3}He	LO	450	−11.34	−11.33	51.45	−62.79		9.851	1.0000	96.24	0.019	3.75	1.342	1.264
	NLO		−7.751	−7.745	33.55	−41.30		5.217	0.9998	94.79	0.027	5.18	1.744	1.579
	N^{2}LO (NN-only)		−7.397	−7.392	34.15	−41.55		4.967	0.9998	93.29	0.043	6.67	1.797	1.620
	N^{2}LO+3NFs		−7.734	−7.729	35.37	−42.65	−0.452	5.26	0.9995	92.57	0.076	7.35	1.766	1.598
^{3}He	LO	500	−11.63	−11.62	56.88	−68.51		10.865	0.9999	94.94	0.036	5.02	1.308	1.237
	NLO		−7.574	−7.568	35.07	−42.65		5.557	0.9997	94.30	0.031	5.67	1.768	1.598
	N^{2}LO (NN-only)		−7.194	−7.188	37.11	−44.30		5.164	0.9995	92.08	0.059	7.86	1.834	1.649
	N^{2}LO+3NFs		−7.739	−7.733	39.44	−46.54	−0.641	5.65	0.9991	91.43	0.107	8.47	1.772	1.602

TABLE II. Summary of energies and wave-function properties for ^{4}He. See text for explanations. Energies and cutoffs are given in MeV. The matter radius r_N is given in fm and the S-, P-, and D-state probabilities are given in %.

		Λ	E	$\langle H\rangle$	$\langle T\rangle$	$\langle V_{NN}\rangle_1$	$\langle V_{NN}\rangle_2$	$\langle V_{3NF}\rangle$	$\langle\Psi\|\Psi\rangle_1$	$\langle\Psi\|\Psi\rangle_2$	P(S)	P(P)	P(D)	r_N
^{4}He	LO	450	−49.99	−49.98	124.4	−174.4	−174.4		0.99952	0.99980	95.71	0.070	4.21	0.990
	NLO		−29.36	−29.34	71.47	−100.8	−100.8		0.99914	0.99932	92.02	0.129	7.84	1.375
	N^{2}LO, NN-only		−27.32	−27.28	71.95	−99.3	−99.2		0.99887	0.99894	89.71	0.211	10.07	1.423
	N^{2}LO+3NFs		−28.62	−28.59	75.73	−102.0	−102.0	−2.376	0.99934	0.99923	86.72	0.462	12.81	1.423
^{4}He	LO	500	−51.47	−51.46	139.2	−190.7	−190.7		0.99943	0.99973	93.73	0.147	6.11	0.955
	NLO		−28.15	−28.12	74.56	−102.7	−102.7		0.99872	0.99863	90.96	0.154	8.87	1.408
	N^{2}LO, NN-only		−25.95	−25.85	78.54	−104.5	−104.4		0.99806	0.99758	87.36	0.303	12.32	1.469
	N^{2}LO+3NFs		−28.72	−28.62	86.71	−111.9	−111.9	−3.474	0.99873	0.99811	85.06	0.597	14.34	1.424

channels into account, there is no contribution from charge-symmetry breaking to the kinetic energy. Also the proton and neutron radii are exactly equal in this approximation.

The pattern of binding is very similar to the $A = 3$ nuclei, as can be seen in Table II. In leading order, there is strong overbinding compared to the experimental ^{4}He binding energy of −28.296 MeV [64]. This is drastically reduced at NLO, leading even to a slight underbinding for $\Lambda = 500$ MeV. At N^{2}LO, ^{4}He is clearly underbound for both cutoffs when only NN interactions are used. Adding the 3NFs then leads to mild overbinding again. The effect of the 3NFs is larger for the larger cutoff. An alternative approach has been proposed [65] which reduces the strong overbinding at LO and it will be interesting to see if that approach is successful when consistent higher orders are developed.

As described in more detail in Ref. [62], the $A = 4$ calculations are solved using two kinds of Jacobi coordinates that either single out a three-nucleon subsystem (3+1) and a spectator nucleon or two two-nucleon subsystems (2+2). It is advantageous to use both kinds of coordinates simultaneously since this allows for the most effective representation of the Yakubovsky components. Again, like in $A = 3$, we perform the normalization of the wave function using overlaps of the Yakubovsky component and the wave function and then calculate the norm using only the wave function in either the 3+1 representation ($\langle\Psi|\Psi\rangle_1$) or in the 2+2 one ($\langle\Psi|\Psi\rangle_2$). As one can see in the table, the deviation from 1 is less than 1% for both representations of the wave function.

We also give the expectation values of the Hamiltonian, the kinetic energy and the potential energy in both representations. In contrast to $A = 3$, there are small deviations between the expectation value $\langle H\rangle$ and E that can not be traced back to additional charge-symmetry breaking contributions in the kinetic energy but are due to the missing isospin $T = 1$ and $T = 2$ components and due to missing higher partial waves in intermediate states. For $A = 3$, such deviations did not show up because all isospin channels were included and because no intermediate steps were necessary to compute wave functions and expectation values.

Table II also compiles the S-, P-, and D-state probabilities, which follow a very similar trend as the ones for $A = 3$. Finally, the point-nucleon matter radius r_N is also given. Again, we observe the expected correlation with the binding energy with the exception that 3NFs can contribute additional binding without decreasing the radius.

We conclude this section with a short discussion on the radii of the $A = 3, 4$ nuclei. The (unobservable) point-proton matter radius r_p quoted in Tables I and II is related to the charge radius r_c by the well-known equation [66]

$$r_c^2 = r_p^2 + R_p^2 + \frac{3}{4m_p^2} + \frac{N}{Z}R_n^2 + r_{\rm so}^2 + r_{\rm mec}^2 + \cdots , \qquad (10)$$

where m_p, R_p, and R_n are the proton mass, charge radius and the neutron charge radius, respectively, while the ellipses refer to higher-order relativistic corrections. Further, $r_{\rm so}^2$ denotes the contribution of the spin-orbit term of relativistic nature, see Refs. [42,67] for more details, while $r_{\rm mec}^2$ refers to the contribution of the exchange charge density. In a close analogy to the deuteron, see, e.g., Ref. [68], one can define the point-proton structure radius $r_{\rm str}$ via

$$r_{\rm str}^2 = r_c^2 - \left(R_p^2 + \frac{3}{4m_p^2} + \frac{N}{Z}R_n^2\right). \qquad (11)$$

This quantity is observable and differs from the point-proton matter radius r_p by taking into account the contributions associated with nuclear binding mechanisms such as $r_{\rm so}^2$ and $r_{\rm mec}^2$. Since these corrections first appear at N^{3}LO, see Refs. [69–71], our N^{2}LO predictions for r_p coincide with the ones for the structure radii, whose experimental values can be extracted from the corresponding charge radii $r_{c,\,^3{\rm H}}^{\rm exp} = 1.755(86)$ fm [72], $r_{c,\,^3{\rm He}}^{\rm exp} = 1.973(14)$ fm [73], and $r_{c,\,^4{\rm He}}^{\rm exp} = 1.681(4)$ fm [74]. Using the CODATA-2018 recommended value for the proton radius, $R_p = 0.8414(19)$ fm [75], along with the current PDG value for the square charge radius of the neutron, $R_n^2 = -0.1161(22)$ fm^2 [76],[3] we extract the corresponding structure radii $r_{{\rm str},\,^3{\rm H}}^{\rm exp} = 1.604(96)$ fm, $r_{{\rm str},\,^3{\rm He}}^{\rm exp} = 1.792(17)$ fm, and $r_{{\rm str},\,^4{\rm He}}^{\rm exp} = 1.484(6)$ fm. Notice that this value for $r_{{\rm str},\,^4{\rm He}}^{\rm exp}$ is significantly (by ≈1.5%) larger than the one of $r_{{\rm str},\,^4{\rm He}}^{\rm exp} = 1.462(6)$ fm given in Ref. [66] and also quoted in our earlier studies [14,31]. This difference is caused entirely by employing the updated (smaller) value for the proton radius recommended by the CODATA group [75], and

[3]Notice, however, that our recent determination of R_n^2 from the atomic isotope shift data [41,42] yielded a somewhat smaller in magnitude value of $R_n^2 = -0.105^{+0.005}_{-0.006}$ fm^2, which would result in slightly smaller structure radii.

TABLE III. Summary of energies for ^{4}He, ^{6}He, and ^{6}Li from LO up through N^{2}LO including 3NFs $\alpha = 0.08$ and 0.04 fm^4. Quoted uncertainties are the extrapolation uncertainties only. Energies and cutoffs are given in MeV. Experimental values are from Refs. [64,78].

^{A}Z(J^π, T)	Λ	α (fm^4)	LO	NLO	N^{2}LO, NN-only	N^{2}LO NN+3NFs	Expt. (MeV)
^{4}He(0^+, 0)	450	0.04	−49.891(2)	−29.339(3)	−27.254(5)	−28.447(4)	−28.296
	450	0.08	−49.733(1)	−29.366(1)	−27.260(2)	−28.527(2)	
	500	0.04	−51.327(1)	−28.087(3)	−25.816(5)	−28.585(5)	
	500	0.08	−51.167(1)	−28.123(2)	−25.807(3)	−28.630(2)	
^{6}He(0^+, 1)	450	0.04	−46.5(5)	−28.73(16)	−27.09(16)	−28.84(20)	−29.27
	450	0.08	−46.7(3)	−27.86(14)	−27.18(10)	−29.04(7)	
	500	0.04	−47.2(6)	−27.27(15)	−25.66(16)	−29.08(20)	
	500	0.08	−47.6(4)	−27.39(10)	−25.69(7)	−29.21(6)	
E_x(2^+, 0)	450	0.08	3.5(9)	2.10(31)	2.09(23)	2.10(15)	1.80
	500	0.08	3.6(1.0)	2.08(23)	2.08(12)	2.08(07)	
^{6}Li(1^+, 0)	450	0.04	−50.1(4)	−31.79(11)	−30.20(16)	−31.85(15)	−31.99
	450	0.08	−50.4(3)	−31.93(9)	−30.28(6)	−32.04(6)	
	500	0.04	−50.7(6)	−30.33(12)	−28.75(15)	−32.17(20)	
	500	0.08	−51.1(3)	−30.45(6)	−28.77(5)	−32.29(4)	
E_x(3^+, 0)	450	0.08	5.3(8)	2.90(17)	2.85(12)	2.40(7)	2.19
	500	0.08	5.1(9)	2.93(14)	2.82(7)	2.41(7)	

consistent with decade-long findings using dispersion theory, see, e.g., Ref. [77].

Our N^{2}LO predictions underestimate the central experimental values for the structure radii of all three considered nuclei. The amount of underestimation is slightly smaller for the larger cutoff $\Lambda = 500$ MeV. This is in line with the recent high accuracy calculations of the deuteron charge and quadrupole form factors [41,42], where the contribution of the two-body short-range charge density was found to decrease with increasing cutoff values. Using the same Bayesian model $\bar{C}^{650}_{0.5-10}$ as employed in Sec. III for 3N scattering observables to estimate the truncation errors for the radii, our N^{2}LO predictions for $\Lambda = 500$ MeV $r^{\rm N2LO}_{\rm str,\,3H} = 1.581(29)$ fm, $r^{\rm N2LO}_{\rm str,\,3He} = 1.772(37)$ fm, and $r^{\rm N2LO}_{\rm str,\,4He} = 1.424(36)$ fm are found to be consistent with the experimental values for the $A = 3$ nuclei. At the 95% Bayesian confidence level corresponding to $r^{\rm N2LO}_{\rm str,\,4He} = 1.424(109)$ fm, our result for ^{4}He is also in agreement with the experimental datum.

V. P-SHELL NUCLEI

We now turn to heavier p-shell nuclei. For simplicity, we ignore the proton-neutron mass difference, and use the same nucleon mass $m = 938.92$ MeV for the protons and the neutrons; furthermore, we add a standard repulsive Coulomb potential between the protons.

We use the No-Core Configuration Interaction (NCCI) approach [79] to determine the ground states of p-shell nuclei (excluding mirror nuclei) at N^{2}LO; for select nuclei we perform calculations at lower orders, and include narrow low-lying excited states as well. In the NCCI approach we expand the wave function Ψ of a nucleus consisting of A nucleons in an A-body basis of Slater determinants Φ_k of single-particle wave functions $\phi_{nljm}(\vec{r})$. Here, n is the radial quantum number, l the orbital motion, j the total spin from orbital motion coupled to the intrinsic nucleon spin, and m the spin-projection. The Hamiltonian $\hat{H}$ is also expressed in this basis and thus the many-body Schrödinger equation becomes a matrix eigenvalue problem; for an NN potential plus 3NFs, this matrix is sparse for $A > 4$. The eigenvalues of this matrix are approximations to the energy levels, to be compared to the experimental binding energies and spectra, and the corresponding eigenvectors to the nuclear wave functions.

We use the conventional harmonic oscillator (HO) basis with energy parameter $\hbar\omega$ for the single-particle wave functions, in combination with a truncation on the total number of HO quanta in the system: the basis is limited to many-body basis states with $\sum_A N_i \leqslant N_0 + N_{\rm max}$, with N_0 the minimal number of quanta for that nucleus and $N_{\rm max}$ the truncation parameter. (Even/odd values of $N_{\rm max}$ provide results for natural/unnatural parity.) Numerical convergence toward the exact results for a given Hamiltonian is obtained with increasing $N_{\rm max}$, and is marked by approximate $N_{\rm max}$ and $\hbar\omega$ independence. In practice, we use extrapolations to estimate the binding energy in the complete (but infinite-dimensional) space [80–84], based on a series of calculations in finite bases.

The rate of convergence depends both on the nucleus and on the interaction. For realistic interactions, the dimension of the matrix needed to reach a sufficient level of convergence is in the tens or even hundreds of billions, which saturates or exceeds the capabilities of current high-performance computing facilities. In order to improve the convergence of the basis space expansion, we therefore first apply a Similarity Renormalization Group (SRG) transformation [85–87] to soften these interactions. Most of the results presented here have been evolved to an SRG parameter of $\alpha = 0.08$ fm^4 and all of them include any induced 3NFs, but we have also performed calculations at $\alpha = 0.04$ fm^4 in order to make sure the dependence on the SRG parameter is weak. For ^{4}He we also compare with the Yakubovsky calculations presented in the previous section.

The calculations described in this section have been performed with the NCCI code MFDn [88,89] to calculate the lowest energy levels with natural parity of p-shell nuclei. Most

NCCI calculations were performed on the IBM BG/Q Mira at the Argonne Leadership Computing Facility (ALCF), with additional calculations performed on the Cray XC40 Theta at ALCF and the Cray XC40 Cori at the National Energy Scientific Computing Center (NERSC). For all nuclei we have performed calculations for at least four $\hbar\omega$ values (one below, and two above the variational minimum), in order to perform extrapolations to the complete (infinite-dimensional) basis with uncertainty estimates. We use a simple three-point exponential extrapolation in $N_{\max}$ at fixed $\hbar\omega$,

$$E^{\hbar\omega}(N_{\max}) = E_{\infty}^{\hbar\omega} + a\, e^{(-b N_{\max})}, \tag{12}$$

using three consecutive values of $N_{\max}$ around the variational minimum in $\hbar\omega$, which seems to work well for a range of interactions and nuclei [80,90,91]. We take as our best estimate for E_∞ in the complete basis the value of $E_{\infty}^{\hbar\omega}$ for which $|E_{\infty}^{\hbar\omega} - E^{\hbar\omega}(N_{\max})|$ is minimal. Our estimate of the extrapolation uncertainty is given by the maximum of

(i) the difference in $E_{\infty}^{\hbar\omega}$ for two successive extrapolations using data for $(N_{\max}-6, N_{\max}-4, N_{\max}-2)$ and $(N_{\max}-4, N_{\max}-2, N_{\max})$, respectively;
(ii) half the variation in $E_{\infty}^{\hbar\omega}$ over a 8-MeV interval in $\hbar\omega$ around the variational minimum;
(iii) 20% of $|E_{\infty}^{\hbar\omega} - E^{\hbar\omega}(N_{\max})|$.

This procedure is identical to what was used in Refs. [16,31]. When we apply this method to ^{3}H, our results are, within the estimated extrapolation uncertainties, in excellent agreement with the Yakubosky results discussed in the previous section, see Table I. As expected, the NCCI calculations performed after SRG evolution to $\alpha = 0.08$ fm^4 converge faster, with estimated extrapolation uncertainties in the ground-state energies of about ten keV, whereas the extrapolation uncertainties are up to about a hundred keV at $\alpha = 0.04$ fm^4. Within these uncertainties, our results are also independent of the SRG parameter α.

In Table III we list our order-by-order results for the ground-state energies of ^{4}He and $A = 6$ nuclei for $\alpha = 0.04$ and 0.08 fm^4. The quoted uncertainties in Table III are the extrapolation uncertainties only. For ^{4}He we can perform these calculations up to $N_{\max} = 14$, which is sufficient to obtain the ground-state energies to within a few keV for both $\alpha = 0.04$ and 0.08 fm^4. We do observe a small dependence on the SRG parameter, of the order of a few tens of keV, which can easily be caused by induced 4-body forces from the SRG evolution which have not been incorporated here. Indeed, compared to the results from the Yakubovsky calculations discussed in the previous section, we see differences of up to about a hundred keV in the binding energies (i.e., up to 0.4%), with the Yakubovsky results being slightly deeper bound, see Table II. This suggests that the missing induced four-body forces would lead to slightly stronger binding, at least in ^{4}He.

For ^{6}He and ^{6}Li our calculations are limited by the number of the input 3NF matrix elements, which in practice means that we can perform calculations up to $N_{\max} = 12$. Clearly, our results are not as precise as for ^{4}He, and in fact, our NCCI extrapolation uncertainties at $\alpha = 0.04$ fm^4 are of the same order of magnitude as the difference between the $\alpha = 0.04$ and $\alpha = 0.08$ fm^4 results, whereas the extrapolation uncertainties at $\alpha = 0.08$ fm^4 are significantly smaller, again as expected. We therefore concentrate on our results with $\alpha = 0.08$ fm^4 for nuclei with $A > 6$.

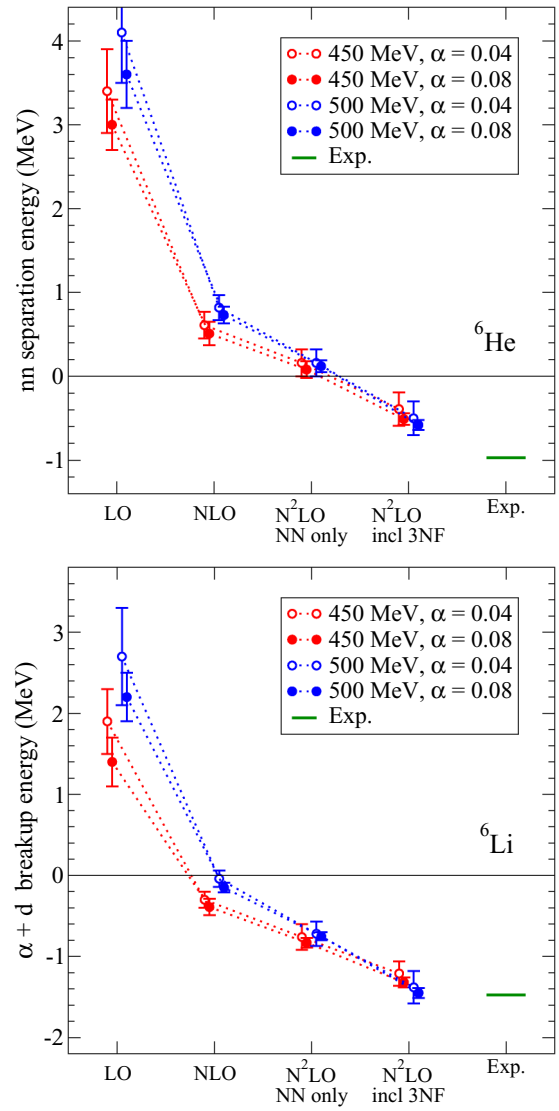

FIG. 5. Order-by-order ^{6}He nn separation energy (top) and ^{6}Li $\alpha + d$ breakup threshold (bottom). Error bars indicate the NCCI extrapolation uncertainties only.

Comparing the results at different chiral orders, we see that there is, not surprisingly, a large difference between the LO and the NLO results, followed by a significantly smaller difference between the NLO and the N^{2}LO predictions. The role of the 3NFs at N^{2}LO is significant, and in fact, while the NN-only potential at N^{2}LO decreases the binding energies by about 1 to 2 MeV compared to the NLO potential, which moves the ground-state energies of ^{6}He and ^{6}Li further away from experiment, with the complete N^{2}LO interaction including the 3NFs the ground-state energies of both ^{6}He and ^{6}Li are within a few hundred keV of the experimental values.

Our results indicate that at LO, neither ^{6}Li nor ^{6}He is bound, as is illustrated in Fig. 5. Here, we calculate the nn separation energy and the $\alpha + d$ breakup threshold as the

TABLE IV. Order-by-order results for ground-state energies of select stable *p*-shell nuclei, with excitation energies for narrow states with natural parity, from LO up through N^{2}LO including 3NFs. Energies and cutoffs are in MeV. Calculated results shown are for $\alpha = 0.08$ fm^4, with the NCCI extrapolation uncertainties only. Experimental values are from Refs. [64,78,92,93].

^{A}Z(J^π, T)	Λ	LO	NLO	N^{2}LO, NN-only	N^{2}LO NN+3NFs	Expt. (MeV)
^{7}Li($\frac{3}{2}^-, \frac{1}{2}$)	450	−61.35(15)	−38.72(9)	−36.98(11)	−39.39(6)	−39.24
	500	−62.1(2)	−36.82(11)	−35.10(14)	−39.73(6)	
E_x($\frac{1}{2}^-, \frac{1}{2}$)	450	−0.07(13)	0.22(11)	0.20(12)	0.32(7)	0.48
	500	−0.09(14)	0.17(12)	0.16(15)	0.35(6)	
E_x($\frac{7}{2}^-, \frac{1}{2}$)	450	10.22(45)	5.54(18)	5.30(23)	4.86(9)	4.63
	500	10.49(60)	5.40(13)	5.05(21)	4.81(8)	
E_x($\frac{5}{2}^-, \frac{1}{2}$)	450	10.10(43)	6.70(16)	6.50(17)	6.65(12)	6.68(5)
	500	10.37(57)	6.37(17)	6.16(18)	6.77(10)	
E_x($\frac{5}{2}^-, \frac{1}{2}$)	450	16.55(50)	8.64(25)	8.16(16)	7.84(11)	7.46
	500	17.3(6)	8.37(16)	7.73(16)	7.79(9)	
^{8}He(0^+, 2)	450	−41.6(9)	−28.2(7)	−27.1(5)	−30.4(2)	−31.41
	500	−41.6(1.0)	−26.3(6)	−25.6(4)	−30.9(2)	
^{8}Li(2^+, 1)	450	−59.5(3)	−39.44(19)	−38.07(19)	−41.23(16)	−41.28
	500	−59.6(4)	−37.24(14)	−36.11(16)	−41.85(15)	
E_x(1^+, 1)	450	0.50(27)	0.90(20)	0.80(23)	1.11(19)	0.98
	500	0.49(41)	0.80(16)	0.72(17)	1.10(18)	
E_x(3^+, 1)	450	4.57(39)	3.00(28)	2.82(27)	2.54(15)	2.26
	500	4.49(48)	2.92(20)	2.68(22)	2.42(15)	
E_x(0^+, 1)	450	−0.71(23)	2.01(22)	2.15(28)	3.04(26)	?
	500	−0.74(26)	2.26(24)	2.04(26)	3.39(27)	
E_x(4^+, 1)	450	10.65(35)	6.52(35)	6.36(33)	6.80(24)	6.54(2)
	500	11.03(45)	6.24(30)	6.05(27)	6.90(23)	
^{10}Be(0^+, 1)	450	−97.7(1.5)	−61.9(6)	−60.8(4)	−66.5(5)	−64.98
	500	−98.1(1.7)	−57.9(6)	−57.3(5)	−67.5(4)	
E_x(2^+, 1)	450	7.6(2.1)	3.5(8)	3.3(5)	3.3(6)	3.37
	500	8.1(2.5)	3.4(7)	3.0(5)	3.2(4)	
E_x(2^+, 1)	450	6.1(1.6)	4.6(9)	4.8(6)	6.3(7)	5.96
	500	6.6(2.0)	4.2(7)	4.4(6)	6.2(6)	
^{10}B(3^+, 0)	450	−92.8(1.6)	−61.1(6)	−60.3(4)	−66.4(4)	−64.75
	500	−92.5(2.0)	−57.0(5)	−57.0(5)	−68.4(4)	
E_x(1^+, 0)	450	0.2(1.7)	1.8(8)	1.6(5)	1.4(6)	0.72
	500	0.2(2.0)	1.5(7)	1.5(5)	1.8(5)	
E_x(1^+, 0)	450	−6.7(1.6)	−1.4(8)	−0.8(5)	1.7(1.0)	2.15
	500	−7.0(2.0)	−1.6(6)	−0.8(5)	2.2(5)	
E_x(2^+, 0)	450	−0.6(1.9)	2.1(6)	2.2(5)	3.4(5)	3.59
	500	−0.8(2.1)	1.6(5)	1.9(5)	4.1(5)	
E_x(3^+, 0)	450	1.5(2.2)	3.8(1.1)	4.2(7)	5.7(7)	4.77
	500	1.3(2.6)	3.3(9)	3.9(5)	7.1(6)	
^{12}B(1^+, 1)	450	−113.7(1.3)	−76.0(7)	−76.7(5)	−84.8(4)	−79.58
	500	−111.7(1.6)	−70.4(6)	−72.6(5)	−87.5(4)	
E_x(2^+, 1)	450	4.4(1.3)	1.2(8)	0.7(5)	−0.9(4)	0.95
	500	4.6(1.7)	1.4(7)	0.6(5)	−1.1(4)	
E_x(0^+, 1)	450	−1.3(1.3)	0.3(9)	0.7(5)	1.9(6)	2.72
	500	−1.4(1.6)	0.1(8)	0.5(5)	2.7(6)	
E_x(2^+, 1)	450	0.0(1.4)	1.8(9)	2.0(6)	3.4(7)	3.76
	500	0.0(1.7)	1.5(8)	1.8(6)	4.1(6)	
E_x(1^+, 1)	450	2.1(1.6)	3.0(8)	3.2(5)	4.9(7)	4.99
	500	2.3(2.0)	2.6(6)	2.9(6)	5.7(6)	
E_x(3^+, 1)	450	4.9(1.4)	3.8(9)	4.1(5)	5.3(7)	5.61
	500	5.2(1.8)	3.6(8)	3.8(5)	6.1(7)	
^{12}C(0^+, 0)	450	−145.0(1.0)	−89.7(5)	−90.0(5)	−98.7(4)	−92.16
	500	−144.6(1.2)	−83.3(5)	−85.0(4)	−101.8(4)	
E_x(2^+, 0)	450	6.9(0.9)	3.4(6)	3.2(4)	4.2(4)	4.44
	500	7.5(1.3)	3.1(6)	2.9(5)	4.5(4)	

TABLE IV. (*Continued*.)

^{A}Z(J^π, T)	Λ	LO	NLO	N^{2}LO, NN-only	N^{2}LO NN+3NFs	Expt. (MeV)
$E_x(1^+, 0)$	450	31.3(1.2)	14.2(6)	12.9(5)	9.6(4)	12.71
	500	32.2(1.4)	13.6(6)	11.8(5)	9.9(4)	
$E_x(4^+, 0)$	450	23.3(1.1)	12.2(7)	11.7(5)	13.7(5)	14.08
	500	24.6(2.0)	11.4(6)	10.8(5)	14.6(4)	

difference between the extrapolated energies of ^{6}He and ^{4}He, and between that of ^{6}Li and $E_\alpha + E_d$, respectively; for the numerical uncertainty we take the extrapolation uncertainty of the $A = 6$ nucleus. It turns out that ^{6}He only becomes bound at N^{2}LO including 3NFs, both with the 450-MeV and the 500-MeV regulator. And even then it is bound relative to ^{4}He by only 0.5 to 0.6 MeV, whereas experimentally it is bound by about 1 MeV. On the other hand, ^{6}Li becomes minimally bound at NLO, and its binding relative to the $\alpha + d$ threshold is in good agreement with the experimental breakup threshold for both regulator values. Note that this is qualitatively similar to what we found in Ref. [31] using the SCS interactions.

In addition to the ground-state energies, we also list in Table III the excitation energies of the lowest excited states in ^{6}He and ^{6}Li at $\alpha = 0.08$ fm^4. For these excitation energies, we extrapolate the total energy of these excited states to the complete (infinite-dimensional) basis, following the same procedure as for the ground states. Next, we take the difference between these extrapolated energies as our best estimate for the excitation energy. For the corresponding extrapolation uncertainties we take the maximum of the estimated extrapolation uncertainties of the total energies of the two states, which is a rather conservative uncertainty estimate given the often strong correlations between different states in the spectrum. For narrow excited states (and we mainly consider narrow excited states in this work), this extrapolation method seems to give results that are numerically reasonably stable, even for states that are above threshold, and has the advantage that we can apply the same method to all nuclei under consideration. Our results clearly indicate (not surprisingly!) that there are strong correlations between the ground state and the excited state—the difference between the excitation energies at different chiral orders is significantly smaller than the difference between the ground-state energies at different chiral orders. We will come back to this when we discuss the uncertainties associated with the truncation of the chiral expansion in the next section. At N^{2}LO, including consistent 3NFs, the excitation energies are within a few hundred keV of the experimental values, which is similar to the deviation of the total ground-state energies from their experimental values. (Our results at $\alpha = 0.04$ fm^4 are within the quoted extrapolation uncertainty estimates, but with larger numerical uncertainties.)

In Table IV we summarize our results for the ground-state energies of a range of p-shell nuclei, as well as the excitation energies for narrow excited states with natural parity (i.e., positive for even nuclei, and negative for odd nuclei in the p shell). We also include the incomplete results at N^{2}LO without the 3NFs in order to highlight the importance of the 3NFs starting at this chiral order. The overall convergence pattern of the ground-state binding energies starts out similar to that of ^{4}He, ^{6}He, and ^{6}Li: significant overbinding at LO, and modest underbinding at NLO. Furthermore, it is interesting to note that for all ground-state energies in Table IV, the difference between N^{2}LO calculations with or without 3NFs is noticeably larger than the difference between NLO and N^{2}LO calculations without 3NFs. This highlights the importance of 3NFs at N^{2}LO.

Looking in more detail at specific nuclei up to $A = 10$, the N^{2}LO NN-only potential leads to even more underbinding than at NLO, but the 3NFs at N^{2}LO increase the binding energy again. The additional binding coming from the 3NFs is significantly stronger with $\Lambda = 500$ MeV than with $\Lambda = 450$ MeV, and overbinds ^{7}Li slightly compared to experiment. Note that for $A = 8$, however, both regulators underbind ^{8}He at N^{2}LO including 3NFs, while the ground-state energy of ^{8}Li is in agreement with experiment for $\Lambda = 450$ MeV (to within the extrapolation uncertainty), and slightly overbound for $\Lambda = 500$ MeV. The amount of overbinding keeps increasing with A; at $A = 10$ the $\Lambda = 450$ MeV interaction also leads to overbinding.

For $A = 12$ the N^{2}LO NN-only potential increases the binding slightly compared to NLO, in contrast to the binding energies up to $A = 10$. Adding the 3NFs leads to significant overbinding for ^{12}C. The overbinding also means that the lowest breakup thresholds appear higher in the spectrum than in reality. In particular, the 3α threshold in ^{12}C is around 15 MeV at N^{2}LO, that is, about a factor of 2 higher than in the real world, as is illustrated in Fig. 6. One would therefore anticipate that the first excited 0^+ in ^{12}C (also known as the Hoyle state), which is experimentally near the 3α threshold, will be significantly too high in the spectrum at N^{2}LO. Unfortunately, within the NCCI approach we cannot correctly describe this state within the numerically accessible basis spaces [94].

As we continue up in the p shell and move to ^{16}O, the amount of overbinding at N^{2}LO gets even worse, as is illustrated in Fig. 7. For comparison, we also include our results with the SCS [31] interaction at N^{2}LO in this figure, which for the considered cutoff values agrees somewhat better with experiment in the upper half of the p shell. The calculated ground-state energies, together with the corresponding experimental values, as well as the deviation from these experimental values, are summarized in Table V.

Next, we show in Fig. 8 the calculated ground-state energies together with the corresponding truncation errors for those nuclei for which the results are available at all orders up through N^{2}LO. Here we use the Bayesian truncation model $\bar{C}^{650}_{0.5-10}$ and assume the expansion parameter $Q = M_\pi^{\rm eff}/\Lambda_b = 200/650 \approx 0.31$. We, however, emphasize that such an estimation is somewhat simplistic, see Ref. [16]

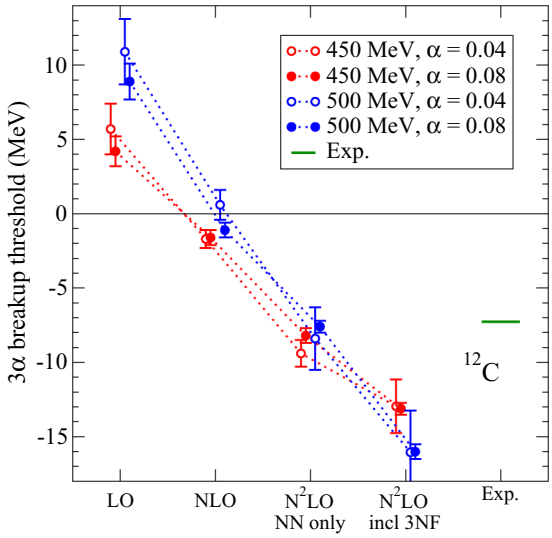

FIG. 6. Order-by-order 3 α breakup threshold of ^{12}C. Error bars indicate the NCCI extrapolation uncertainties only.

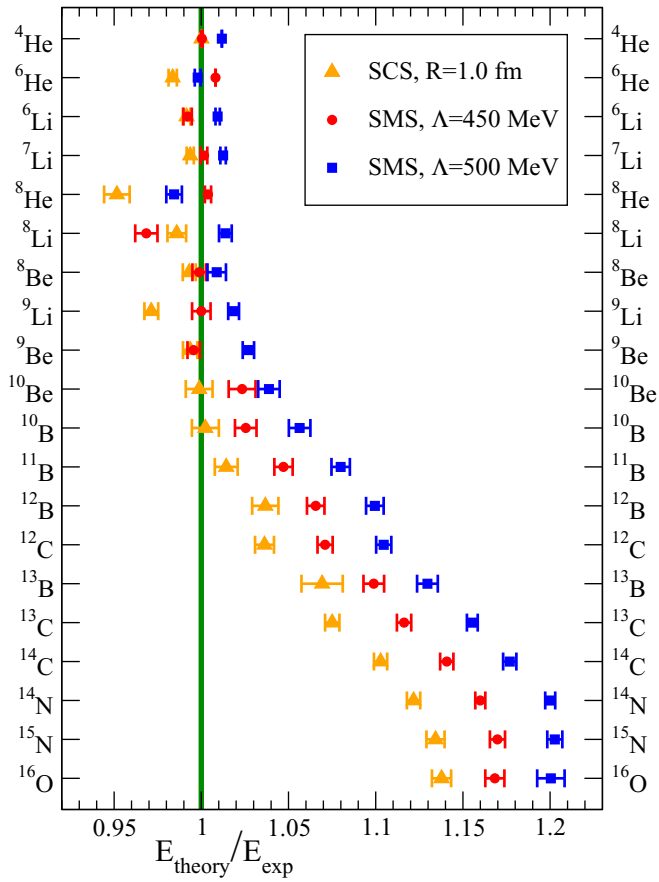

FIG. 7. Comparison of ground-state energies of *p*-shell nuclei between chiral EFT calculations at N^{2}LO and experiment. All results shown are for $\alpha = 0.08$ fm^4 and error bars indicate the NCCI extrapolation uncertainties only.

TABLE V. ground-state energies of *p*-shell nuclei, excluding mirror nuclei, at N^{2}LO including 3NFs with SRG $\alpha = 0.08$ fm^4, together with the deviations from the experimental values. Quoted uncertainties are the extrapolation uncertainties only. Energies and cutoffs are in MeV. Experimental values are from Ref. [64].

^{A}Z(J^π, T)	N^{2}LO(450)	N^{2}LO(500)	Expt. (MeV)
^{4}He(0^+, 0)	−28.527(2)	−28.630(2)	−28.296
	+0.231(2)	+0.334(2)	
^{6}He(0^+, 1)	−29.04(7)	−29.21(6)	−29.27
	−0.23(7)	−0.06(6)	
^{6}Li(1^+, 0)	−32.04(6)	−32.29(4)	−31.99
	+0.05(6)	+0.30(4)	
^{7}Li($\frac{3}{2}^-$, $\frac{1}{2}$)	−39.39(6)	−39.73(6)	−39.24
	+0.15(6)	+0.49(6)	
^{8}He(0^+, 1)	−30.4(2)	−30.9(2)	−31.41
	−1.0(2)	−0.5(2)	
^{8}Li(2^+, 0)	−41.23(16)	−41.85(15)	−41.28
	−0.05(16)	+0.57(15)	
^{8}Be(0^+, 0)	−56.5(3)	−57.0(3)	−56.50
	0.0(3)	+0.5(3)	
^{9}Li($\frac{3}{2}^-$, $\frac{3}{2}$)	−45.14(16)	−46.18(16)	−45.34
	−0.20(16)	+0.84(16)	
^{9}Be($\frac{3}{2}^-$, $\frac{1}{2}$)	−58.82(21)	−59.73(16)	−58.16
	+0.66(21)	+1.57(16)	
^{10}Be(0^+, 1)	−66.5(5)	−67.5(4)	−64.98
	+1.5(5)	+1.5(4)	
^{10}B(3^+, 0)	−66.4(4)	−68.4(4)	−64.75
	+1.7(4)	+3.7(4)	
^{11}B($\frac{3}{2}^-$, $\frac{1}{2}$)	−79.8(4)	−82.3(4)	−76.21
	+3.6(4)	+6.1(4)	
^{12}B(1^+, 1)	−84.8(4)	−87.5(4)	−79.58
	+5.2(4)	+7.9(4)	
^{12}C(0^+, 0)	−98.7(4)	−101.8(4)	−92.16
	+6.5(4)	+9.6(5)	
^{13}B($\frac{3}{2}^-$, $\frac{3}{2}$)	−92.8(5)	−95.4(5)	−84.45
	+8.4(5)	+11.0(5)	
^{13}C($\frac{1}{2}^-$, $\frac{1}{2}$)	−108.3(4)	−112.2(4)	−97.11
	+11.2(4)	+15.1(4)	
^{14}C(0^+, 1)	−120.1(4)	−123.9(4)	−105.28
	+14.8(4)	+18.6(4)	
^{14}N(1^+, 0)	−121.4(4)	−125.6(4)	−104.66
	+16.7(4)	+20.9(4)	
^{15}N($\frac{1}{2}^-$, $\frac{1}{2}$)	−135.1(5)	−138.9(5)	−115.49
	+19.6(5)	+23.4(5)	
^{16}O(0^+, 0)	−149.1(7)	−153.2(1.0)	−127.62
	+21.5(7)	+25.6(1.0)	

and the discussion in the next section. Also, the assumed value for the expansion parameter may be too optimistic for heavier nuclei. This is, e.g., indicated by the spread between the (obviously correlated) predictions for the ground-state energies for $\Lambda = 450$ and 500 MeV in Fig. 7, which can serve as a measure of the N^{2}LO truncation errors (at some low confidence level) and appears to show a clear tendency of increasing with growing values of A. Extending the calculations to N^{3}LO will allow us in the future to perform a more reliable and elaborate estimation of the truncation uncertainty.

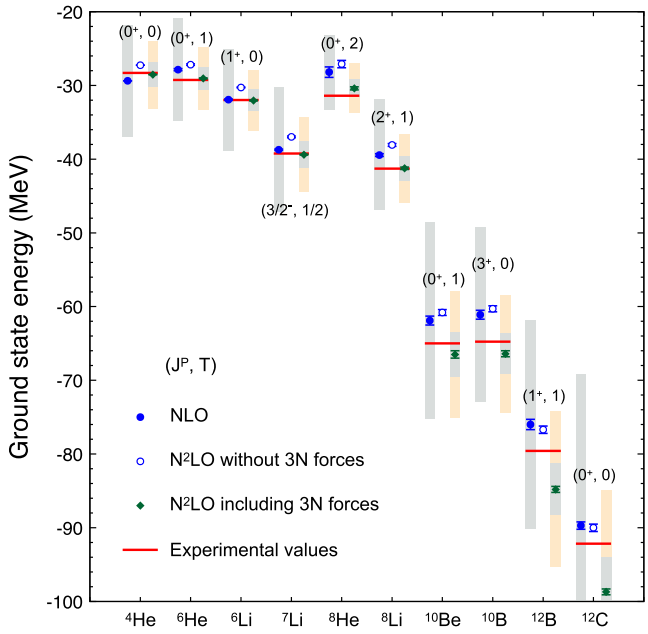

FIG. 8. Calculated ground-state energies in MeV using chiral NLO, and N^{2}LO interactions at $\Lambda = 450$ MeV (blue and green symbols) in comparison with experimental values (red levels). For each nucleus the NLO, and N^{2}LO results are the left and right symbols and bars, respectively. The open blue symbols correspond to incomplete calculations at N^{2}LO using NN-only interactions. Blue and green error bars indicate the NCCI extrapolation uncertainty. All results shown are for $\alpha = 0.08$ fm^4. The light (coral) and dark (gray) shaded bars indicate the 95% and 68% DoB truncation errors, respectively, estimated using the Bayesian model $\bar{C}^{650}_{0.5-10}$ (at NLO we only show the 68% DoB truncation errors because the 95% errors would be off one or even both ends of the scale).

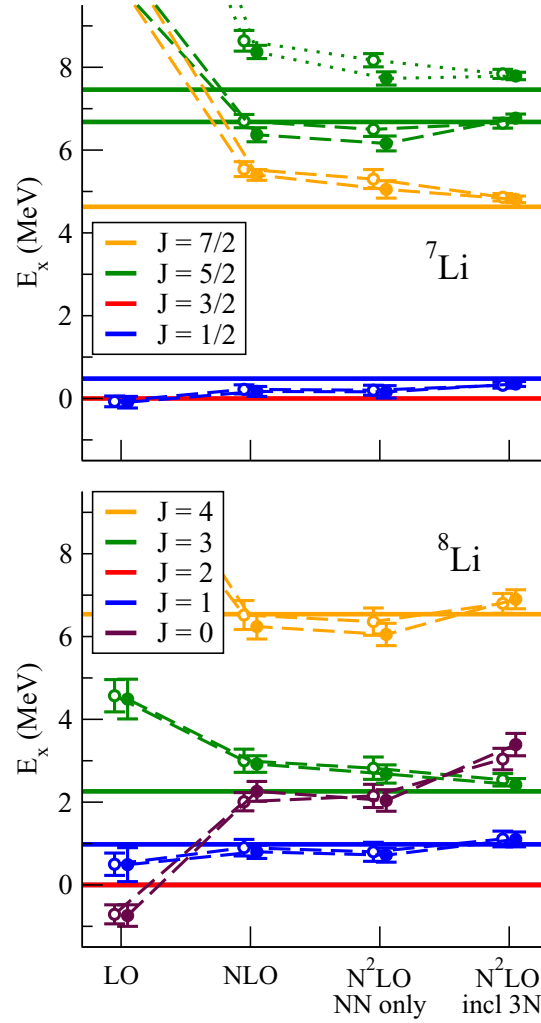

FIG. 9. Order-by-order excitation spectra of ^{7}Li (top) and ^{8}Li (bottom). All excitation energies are obtained with SRG parameter $\alpha = 0.08$ fm^4; open symbols are with $\Lambda = 450$ MeV, closed symbols are with $\Lambda = 500$ MeV, and horizontal lines indicate experimental values [78,92]. Dashed (dotted) lines connect results for the lowest (second) excited state of a given J at different orders.

In Table IV we also list our order-by-order results for the excitation energies. Again, these excitation energies are the difference of the extrapolated total energies. For ^{7}Li our results are, starting from NLO, in good qualitative agreement with experiment, see Fig. 9. However, at LO the spectrum looks very different: The ground state and first excited state are nearly degenerate, and reversed in order, while the second and third excited state are significantly too high and also nearly degenerate. This can easily be qualitatively explained in terms of the clustering: the lowest two states in ^{7}Li can be viewed as a bound states of ^{3}H and ^{4}He in an $L = 1$ state with the spin and orbital motion (anti)aligned, whereas the second and third excited state are bound states of ^{3}H and ^{4}He in an $L = 3$ state with the spin and orbital motion (anti)aligned. Without sufficient spin-orbit splitting in the NN-potential at LO, the first two states become degenerate, as do the second and third state. Note that the second excited $\frac{5}{2}^-$ state has a different structure, and is even higher in the spectrum at LO. Starting from NLO, however, the spectrum is in qualitative agreement with experiment, and the differences between the excitation energies between NLO and N^{2}LO (with or without 3NFs) are less than an MeV; and at N^{2}LO (with 3NFs) there is good agreement with the experimental values.

Also for ^{8}Li we see a qualitative difference between the spectrum at LO and at higher orders: at LO the ground state is actually a 0^+ state, whereas the experimental ground state is a 2^+ state. (Note that there is no narrow 0^+ listed in Ref. [92].) Starting from NLO, the excitation energies of the 1^+, 3^+, and 4^+ states are in reasonable agreement with the known experimental values, with only small changes as one goes from NLO to N^{2}LO without and with 3NFs; the latter gives best agreement for the low-lying spectrum. In addition to the known narrow 1^+, 3^+, and 4^+ states, and the 0^+ state which is the ground state at LO, we also see evidence for additional 1^+ and 2^+ states between 3 and 7 MeV at N^{2}LO with 3NFs. These states are also found with the SCS interactions [95]; however, they are not very well converged and probably correspond to broad resonances.

The two lowest excited states of ^{10}Be are both $J = 2$ states, and at N^{2}LO their excitation energies are in good agreement

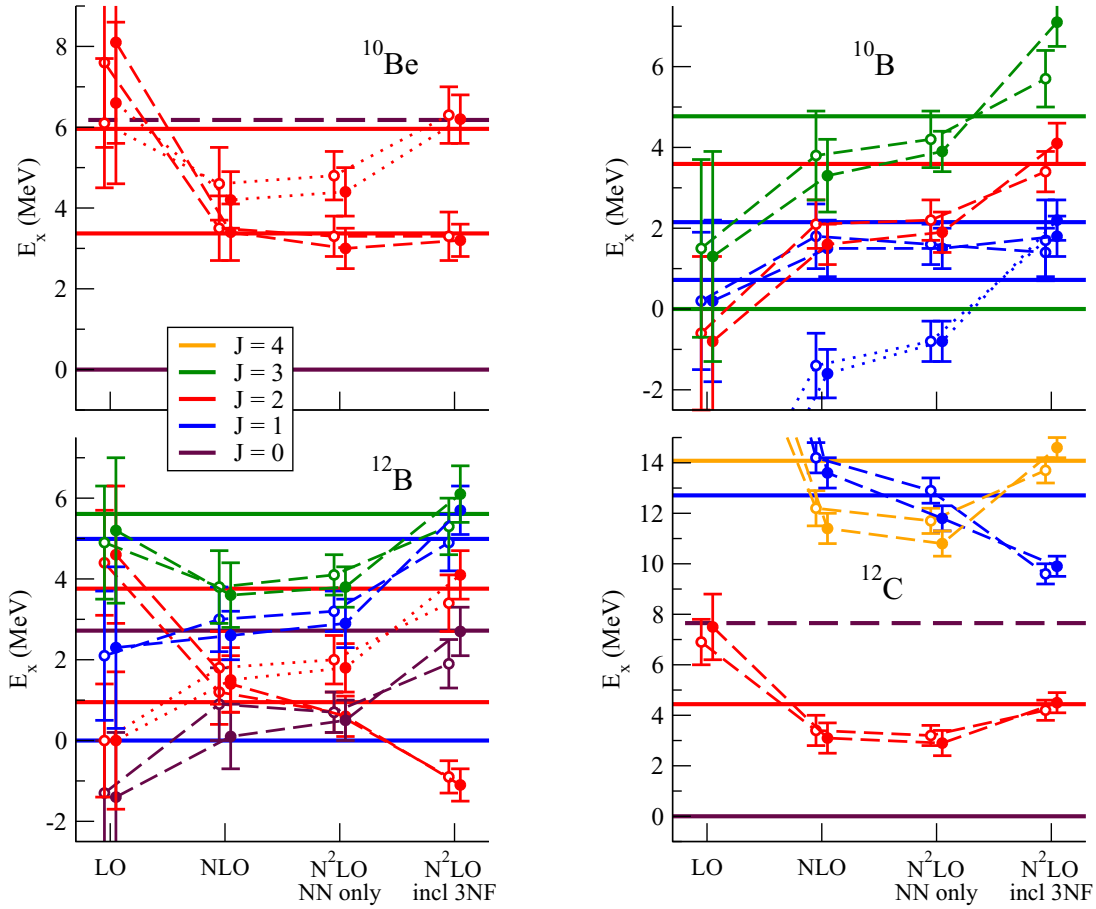

FIG. 10. Order-by-order excitation spectra of ^{10}Be (top left), ^{10}B (top right), ^{12}B (bottom left), and ^{12}C (bottom right). All excitation energies are obtained with SRG parameter $\alpha = 0.08$ fm^4; open symbols are with $\Lambda = 450$ MeV, closed symbols are with $\Lambda = 500$ MeV. Dashed (dotted) lines connect results for the lowest (second) excited state of a given J at different orders. Horizontal lines indicate experimental values [92,93]; the horizontal dashed lines indicate excited 0^+ states in ^{10}Be and ^{12}C not in the low-lying spectra of our NCCI calculations.

with the experimental values, see Fig. 10. Although they have the same quantum numbers, they are easily distinguished by their quadrupole moments: at N^{2}LO the first $J = 2$ state has a negative quadrupole moment and can be identified as a rotational excitation of the ground state [96], whereas the second $J = 2$ has a positive quadrupole moment. Note, however, that at LO the order of these two states is reversed. In addition to these two $J = 2$ states, there is also a narrow $J = 0$ excited state at 6.179 MeV (see Ref. [92]), for which we do not find any evidence in our NCCI calculations. It is unclear whether that is a deficiency of the NCCI approach or a property of the interaction; also with the SCS interactions we do not see this excited $J = 0$ state in the low-lying spectrum [31,95].

The low-lying spectrum of ^{10}B is known to be very sensitive to details of the interaction, and in particular to 3NFs [97]. Indeed, in Fig. 10 we see that without 3NFs we do not get the correct ground state: one of the two low-lying $J = 1$ states is (well) below the lowest $J = 3$ state at LO, NLO, and N^{2}LO without 3NFs. Only after adding the 3NFs at N^{2}LO do we get the correct ground state, and what appears to be the ground state at lower orders, seems to become the second $J = 1$ state, based on observables such as the magnetic and quadrupole moments (dotted line in Fig. 10). A complicating factor is that the two low-lying $J = 1$ states mix as function of the basis parameters $\hbar\omega$ and $N_{\max}$, which makes the extrapolation to the complete basis less reliable. Nevertheless, at N^{2}LO with 3NFs we find reasonable agreement for the low-lying spectrum, given our numerical uncertainty estimates. Furthermore, it is interesting to note that the convergence pattern with chiral order, and the effect of the 3NFs, is very similar for the $J = 1$ state that is lowest at LO and NLO (dotted line), the $J = 2$ state, and the first excited $J = 3$ state, indicating strong correlations between these three states.

The spectrum of ^{12}B turns out to be even more sensitive to the NN and 3N interaction, as can be seen in the lower-left panel of Fig. 10. There are two narrow $J = 2$ excited states in ^{12}B, which have an opposite behavior as we go from LO to N^{2}LO in the chiral expansion: one of them is almost degenerate with the $J = 1$ ground state at LO, but its excitation energy increases at NLO, and increases further at N^{2}LO (including 3NFs), whereas the excitation energy of the second $J = 2$ state at LO decreases at higher orders, and this $J = 2$ state drops below the physical $J = 1$ ground state at N^{2}LO with 3NFs, becoming (incorrectly) the predicted ground state. Also note that there are three excited states, with $J = 0$, 1, and 2, whose excitation energies have a very similar pattern as

function of the chiral order—and this pattern is also very similar to that seen for three low-lying states in ^{10}B. This suggests that these states have a closely related structure, which deserves further investigation. It also remains to be seen what happens at higher chiral orders.

Finally, the spectrum of ^{12}C. As already mentioned, the Hoyle state (the first excited $J = 0$ state in ^{12}C, which is near the 3α threshold) cannot be correctly described within the NCCI approach within the numerically accessible basis space. In Fig. 10 this state is represented by the dashed line. The $J = 2$ and $J = 4$ states are rotational excitations of the ground state [98], and it is therefore no surprise that their behavior as a function of the chiral order is very similar; the ratio of their respective excitation energies remains nearly constant at about 3.3, as one would expect for a rotational band. More interesting and puzzling is the systematic decrease with chiral order of the $J = 1$ (with $T = 0$) state, in particular with the inclusion of the 3NFs at N^{2}LO. Again, the question is what happens with this state at higher chiral orders.

To summarize, most of the calculated spectra of p-shell nuclei show good agreement with experiment for the lowest narrow states with natural parity, with only a few exceptions. These exceptions are the $J = 0^+$ excited states in ^{10}Be and ^{12}C (which are most likely absent in our calculations due to the limited basis spaces), as well as several states that are particularly sensitive to the details of the NN-potential and the 3NFs. Specifically, these are the excited $J = 1$ state in ^{12}C; the $J = 2$ state in ^{12}B, which is the second excited $J = 2$ state at LO and NLO, but which becomes the theoretical ground state at N^{2}LO, whereas the experimental ground state has $J = 1$; and the lowest states in ^{10}B, which has experimentally a $J = 3$ ground state, with two low-lying $J = 1$ excited states, but in ab initio calculations without 3NFs, typically one of these $J = 1$ states becomes the lowest state. However, in order to judge whether or not these exceptions are problematic, we need to consider not only the extrapolation uncertainties, but also the chiral truncation uncertainties.

VI. CORRELATED TRUNCATION UNCERTAINTIES FOR NUCLEAR SPECTRA

In this section we consider the EFT truncation errors for the calculated spectra summarized in Tables III and IV. As described in Sec. III, these uncertainties can be estimated using a Bayesian statistical model that learns from the order-by-order convergence pattern. This model has been applied in Secs. III and IV in a *pointwise* form, meaning that different observables are treated as statistically independent. If applied to the energy spectra from the last section, one would add individual errors in quadrature to find the error bars for excitation energies (because they are a difference between excited- and ground-state energies treated independently). But as already noted and from all other experience, these excitation energies are generally much better determined than energies of the individual levels. Therefore, to avoid overestimating the truncation errors it is essential to apply a *correlated* error model, which we do here.

An extended model applicable to correlated truncation errors was recently developed in Ref. [99] and applied to infinite matter in Refs. [100,101]. This model employed Gaussian processes (GPs) because the observables were continuous functions of the input variables, namely energy and density, respectively. The spectra here are discrete, but we can adapt the GP results because every finite number of inputs will have a joint Gaussian distribution. Rather than learn the hyperparameters of a covariance function that depends on the continuous distance between inputs, we can learn the covariance structure between discrete energy levels and nuclei from the observed pattern of order-by-order expansion coefficients c_i [defined in Eq. (6)].

To manifest the correlations, we plot the c_i coefficients for each individual level listed in Tables III and IV in Fig. 11. For this rough visualization, we extract the c_is using a fixed $Q = M_\pi^{\rm eff}/\Lambda_b = 200/650 \approx 0.31$ for all the states, with $X_{\rm ref}$ taken from experiment (or the N^{2}LO result for the 0^+ state in ^{8}Li). We see high correlation as expected between observable coefficients for the spectra of a given nucleus but also between nuclei. To model these correlations, we introduce a covariance matrix and determine it empirically [102]. We emphasize that the correlations shown beyond c_0 are for the *corrections* to the observables.

As already seen in Eqs. (6) and (7), the truncation error model is contingent on the expansion parameter Q and the characteristic variance $\bar{c}^2$ of the observable expansion coefficients c_i. Ideally we would learn Q^2 and $\bar{c}^2$ from the order-by-order calculations together with the prior expectations for each. A complication for the spectra of light nuclei is that the order-by-order convergence pattern is obscured for those observables at low orders by the strong cancellation between kinetic and potential energies [16]. This is exacerbated in the present case by only having orders up to N^{2}LO.

As a first approach we bypass the problem with the low orders by using just the c_3 coefficients to learn $\bar{c}^2$. By "learning" we mean obtaining a statistical solution to the inverse problem of determining the distribution the coefficients come from (which is characterized by $\bar{c}^2$). We follow Appendix A of Ref. [99] and use a hierarchical model that is computationally efficient and enables us to both parametrize our prior expectations and easily marginalize (i.e., integrate over) the hyperparameters to reduce sensitivity. Previous work has shown little sensitivity to the choice of prior once higher orders are available. With only up to N^{2}LO available we can expect more sensitivity here, but this will be cured in future work with N^{3}LO and higher, so we do not exhaustively test the dependence on the choice of prior. For the analysis of spectra we use the scaled inverse-χ^2 conjugate prior proposed in Ref. [99], which is shown in Fig. 12 for several candidate choices of the hyperparameters ν_0 and τ_0 to assess sensitivity. Based on these tests we have chosen $\nu_0 = 1.5$, $\tau_0 = 1.5$ for the present error analysis.

If we use just the c_3 coefficients but from all of the energy levels to find a posterior for Q (without accounting for correlations), it peaks close to the value adopted for Fig. 11 ($Q \approx 0.3$), which is an average of the somewhat smaller values found for the lighter nuclei and the somewhat larger values found for the heavier nuclei. This is consistent with expectations that Q should increase with the increasing average kinetic energy (the use of the nonobservable kinetic energy

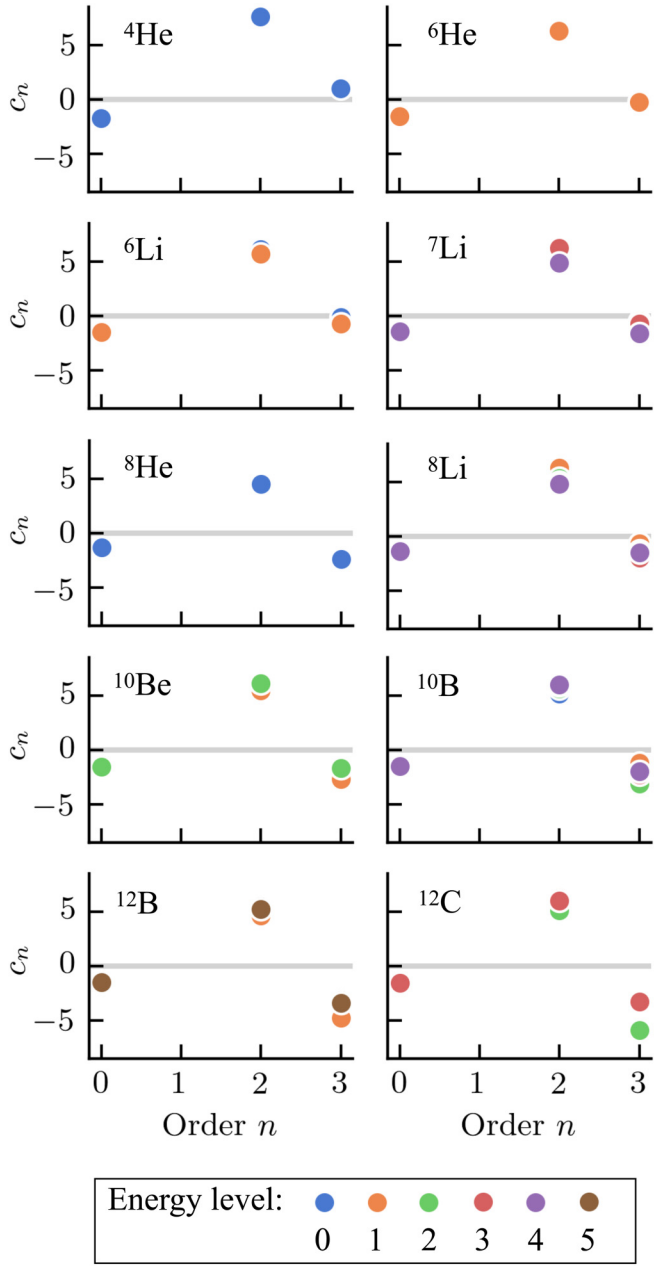

FIG. 11. Expansion coefficients for the individual energy levels in Tables III and IV with $\alpha = 0.08$ fm^4 and $\Lambda = 450$ MeV. These are extracted according to Eq. (9) with a fixed value of $Q \approx 0.31$ and X_{ref} taken from experiment [78,92,93] (or the N^{2}LO result for the 0^+ in ^{8}Li).

in estimating Q is discussed in Ref. [16]). To fit the empirical covariance matrix, it is not sufficient to use the c_3 results. As a start, we also include c_2 for determining the covariance, which might overestimate the degree of correlation based on a comparison of orders in Fig. 11. Other strategies for determining correlations for energy spectra will be explored in future work.

The resulting Bayesian 95% confidence intervals for the excitation energies are shown in Fig. 13, where we plot the difference of theory and experiment. The intervals are shown for

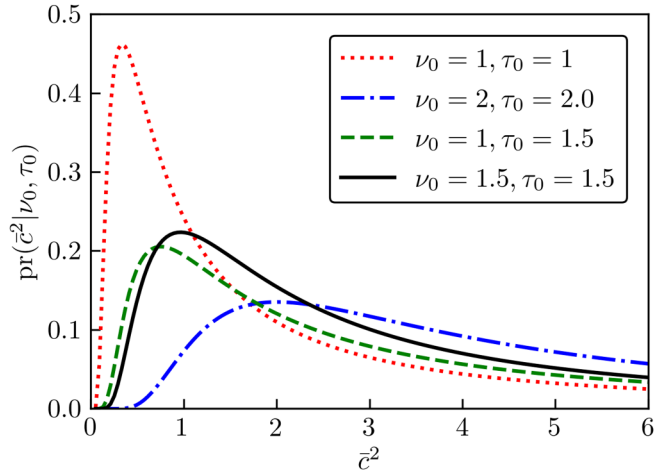

FIG. 12. Prior pdf for the variance $\bar{c}^2$ of the expansion coefficient with several choices of hyperparameters ν_0 and τ_0.

the results from Tables III and IV for both the $\Lambda = 450$ MeV (upper, blue) and $\Lambda = 500$ MeV (lower, red) potentials at SRG $\alpha = 0.08$ fm^4. We see that the uncertainties for the 500 MeV potential are systematically larger than those for 450 MeV potential, but in both cases the empirical coverage of experiment is good. That is, the error bars encompass unity at roughly the rate one would expect for 95% intervals. We emphasize that without taking correlations into account, the intervals would have been significantly larger, and therefore would have been too conservative based on this comparison (i.e., with poor empirical coverage).

When N^{3}LO results are available, we will be able to validate these results and explore the covariance structure in greater detail. It will be interesting to analyze the correlations among states with similar and distinct characteristics as expected from theoretical considerations. We will also seek to make use of the lower-order results along the lines discussed in Ref. [16] as alternative approaches to the truncation errors.

VII. SUMMARY AND CONCLUSIONS

In this paper we have, for the first time, applied the novel SMS chiral NN potentials of Ref. [32], along with the consistently regularized 3NFs comprising subtraction terms, to study selected observables in Nd elastic scattering and the deuteron breakup process as well as various properties of light nuclei up to N^{2}LO in chiral EFT. Our main findings can be summarized as follows:

(i) We have used the approach introduced and advocated in Ref. [31] to determine the LECs c_D and c_E entering the leading 3NF using the triton binding energy and the Nd cross-section minimum at $E_N = 70$ MeV for the cutoff values of $\Lambda = 450$ and 500 MeV. The resulting values of these LECs are found to be of natural size. The predicted results for Nd scattering observables sensitive to the 3NF that have been considered in Ref. [31], namely the doublet scattering length ^2a, Nd total cross section and the differential

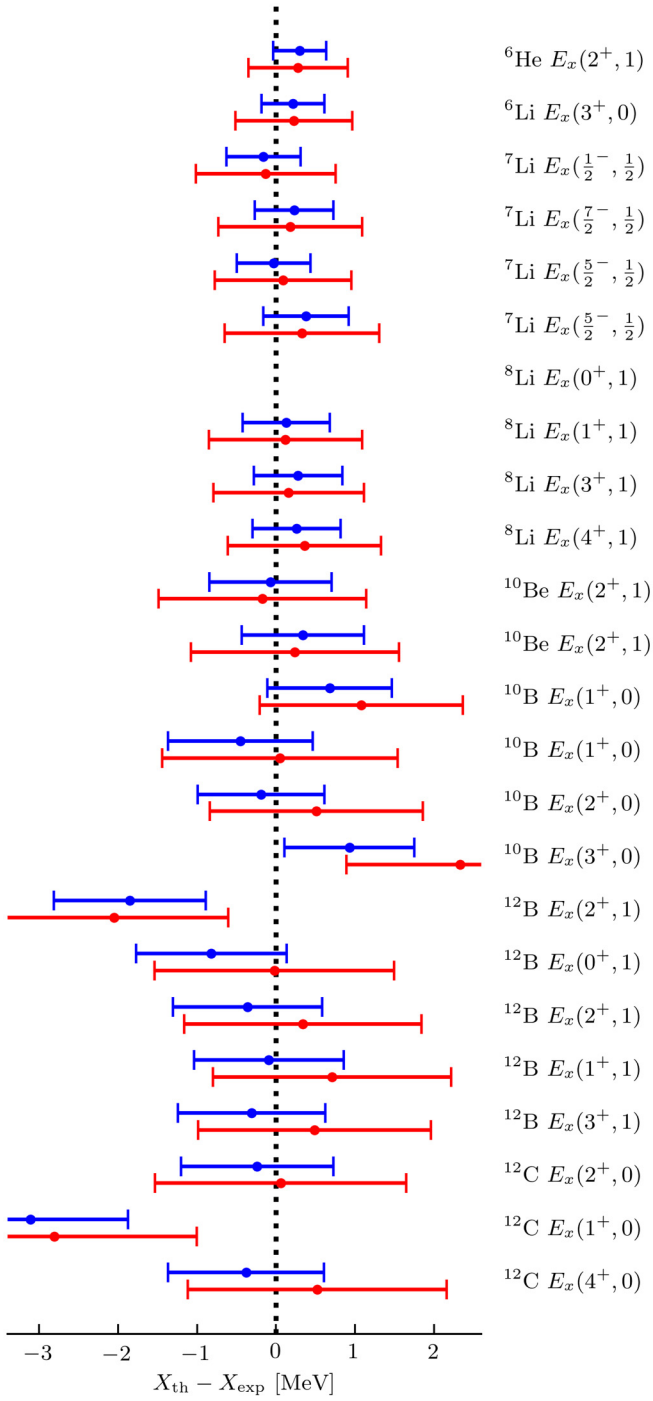

FIG. 13. Central values (dots) for the difference of predicted (at N^{2}LO with 3NFs) and measured excitation energies from Tables III and IV, with 95% Bayesian confidence intervals (for truncation errors only) indicated as error bars. We omit the 0^+ in ^{8}Li because an experimental value is not available and note that the lowest 2^+ in ^{12}B is incorrectly predicted to be the ground state. For each excitation from the calculated ground state, the upper (blue) bar is for $\Lambda = 450$ MeV and the lower (red) bar is for $\Lambda = 500$ MeV. All results shown are for $\alpha = 0.08$ fm^4.

cross section in elastic Nd scattering in the minimum region at $E_N = 108$ and 135 MeV, are found to be in agreement with the experimental data from Refs. [47,54,55]. The only exception are the data of Ref. [47] at $E_N = 135$ MeV, for which a slight discrepancy (at the level of $\approx 1.5\sigma$ is observed). Further, in line with earlier studies, our results suggest that ^2a is not suitable for the determination of these LECs when used in combination with the ^{3}H binding energy due to the well-known strong correlation between these two observables. Our predictions for the considered analyzing powers in elastic Nd scattering at $E_N = 70$ MeV as well as for the differential cross section and nucleon vector analyzing power A_y in selected deuteron breakup configurations at $E_N = 65$ MeV are in reasonable agreement with the data. We demonstrated the agreement between complete N^{2}LO predictions based on the SCS force [31], a previous form of the SMS interaction [38], and on the newly used SMS potential comprising subtraction terms in the 3NFs.

(ii) For the ground-state energies of light nuclei, we observe a similar pattern to the one reported in our earlier study [31] using the SCS chiral interactions at the same chiral order. In particular, while the predicted binding energies are found to be within $\approx 3\%$ of the experimental values for light nuclei, a systematic overbinding trend sets in for $A \sim 9$–10 and increases with growing A. For the considered nuclei up to $A = 12$, our predictions are consistent with the experimental values within errors. For the lightest nuclei with $A = 3, 4$ we have also calculated the point-proton and point-neutron radii. Our predictions for the point-proton structure radii for ^{3}H and ^{3}He agree with the data within errors. For ^{4}He, our N^{2}LO prediction for the radius is $\approx 4\%$ smaller than the central experimental value, but it is still consistent with the datum at the 95% confidence level.

(iii) We have addressed the question of quantifying truncation errors for strongly correlated observables, such as the excitation energy spectra, by using a correlated Bayesian error model and empirically determining the corresponding covariance matrix. Our results for the excitation energies are statistically consistent with both the assumed expansion parameter and the experimental data for the spectra.

In the future, we plan to extend these results in various directions. First, it would be interesting to relax the constraint of exactly reproducing the ^{3}H binding energy employed in all our calculations at N^{2}LO. This would require a more careful uncertainty analysis in the determination of the LECs c_D, c_E that would take into account the expected truncation error for this observable. We also plan to investigate the origin of the overbinding found for heavier nuclei. In particular, it remains to be seen whether this issue is related to deficiencies of the N^{2}LO approximation to the NN force or has to be resolved by higher-order 3NF contributions.

Clearly, the most important step is the extension of these studies to N^{3}LO, which will require the inclusion of the corresponding corrections to the 3NF. However, it was shown in Ref. [3] that one cannot apply the simple regularization

approach we are using in this study to the N^{3}LO contributions derived in Refs. [24–26] using dimensional regularization, as this would destroy consistency with the NN interactions. Rather, all loop contributions to the 3NF (and to exchange charge and current operators) need to be rederived using a consistent semilocal regulator instead of the dimensional regularization. Work along these lines is in progress.

ACKNOWLEDGMENTS

This work was supported by BMBF (Contracts No. 05P18PCFP1 and No. 05P18RDFN1), by the DFG SFB 1245 (Projektnummer 279384907), by the Deutsche Forschungsgemeinschaft (DFG) (Project-ID 196253076 - TRR 110), by the VolkswagenStiftung (Grant No. 93562), by the Polish National Science Center under Grants No. 2016/22/M/ST2/00173 and No. 2016/21/D/ST2/01120, by the US National Science Foundation under Grant No. NSF PHY–1913069, and by the US Department of Energy under Grants No. DE-FG02-87ER40371, No. DE-SC0018223, No. DE-SC0018083, and No. DE-SC0015376. This research used resources of the National Energy Research Scientific Computing Center (NERSC) and the Argonne Leadership Computing Facility (ALCF), which are US Department of Energy Office of Science user facilities, supported under Contracts No. DE-AC02-05CH11231 and No. DE-AC02-06CH11357, and computing resources provided under the INCITE award "*Ab-initio* Nuclear Structure and Nuclear Reactions" from the US Department of Energy, Office of Advanced Scientific Computing Research. Further computing resources were provided on LICHTENBERG at the TU Darmstadt and on JURECA and the JURECA Booster of the Jülich Supercomputing Center, Jülich, Germany.

[1] E. Epelbaum, H.-W. Hammer, and Ulf.-G. Meißner, Rev. Mod. Phys. **81**, 1773 (2009).
[2] R. Machleidt and D. Entem, Phys. Rep. **503**, 1 (2011).
[3] E. Epelbaum, H. Krebs, and P. Reinert, Front. Phys. **8**, 98 (2020).
[4] H.-W. Hammer, S. König, and U. van Kolck, Rev. Mod. Phys. **92**, 025004 (2020).
[5] A. Tichai, R. Roth, and T. Duguet, Front. in Phys. **8**, 164 (2020).
[6] L. E. Marcucci, J. Dohet-Eraly, L. Girlanda, A. Gnech, A. Kievsky, and M. Viviani, Front. Phys. **8**, 69 (2020).
[7] I. Tews, Z. Davoudi, A. Ekström, J. D. Holt, and J. E. Lynn, J. Phys. G **47**, 103001 (2020).
[8] M. Piarulli and I. Tews, Front. Phys. **7**, 245 (2020).
[9] R. Lazauskas and J. Carbonell, Front. Phys. **7**, 251 (2020).
[10] D. Lee, Front. Phys. **8**, 174 (2020).
[11] S. Gandolfi, D. Lonardoni, A. Lovato, and M. Piarulli, Front. Phys. **8**, 117 (2020).
[12] V. Somà, Front. in Phys. **8**, 340 (2020).
[13] H. Hergert, Front. Phys. **8**, 379 (2020).
[14] S. Binder *et al.* (LENPIC Collaboration), Phys. Rev. C **93**, 044002 (2016).
[15] P. Maris *et al.*, EPJ Web Conf. **113**, 04015 (2016).
[16] S. Binder *et al.* (LENPIC Collaboration), Phys. Rev. C **98**, 014002 (2018).
[17] E. Epelbaum, H. Krebs, and U. Meißner, Eur. Phys. J. A **51**, 53 (2015).
[18] E. Epelbaum, H. Krebs, and U. G. Meißner, Phys. Rev. Lett. **115**, 122301 (2015).
[19] E. Epelbaum, W. Glöckle, and U.-G. Meißner, Nucl. Phys. A **747**, 362 (2005).
[20] D. R. Entem and R. Machleidt, Phys. Rev. C **68**, 041001(R) (2003).
[21] D. R. Entem, R. Machleidt, and Y. Nosyk, Phys. Rev. C **96**, 024004 (2017).
[22] R. Skibiński, J. Golak, K. Topolnicki, H. Witała, E. Epelbaum, H. Krebs, H. Kamada, Ulf-G. Meißner, and A. Nogga, Phys. Rev. C **93**, 064002 (2016).
[23] R. Skibiński, J. Golak, K. Topolnicki, H. Witała, E. Epelbaum, H. Kamada, H. Krebs, U.-G. Meißner, and A. Nogga, Few Body Syst. **58**, 28 (2017).
[24] S. Ishikawa and M. R. Robilotta, Phys. Rev. C **76**, 014006 (2007).
[25] V. Bernard, E. Epelbaum, H. Krebs, and Ulf.-G. Meißner, Phys. Rev. C **77**, 064004 (2008).
[26] V. Bernard, E. Epelbaum, H. Krebs, and Ulf.-G. Meißner, Phys. Rev. C **84**, 054001 (2011).
[27] H. Krebs, A. Gasparyan, and E. Epelbaum, Phys. Rev. C **85**, 054006 (2012).
[28] L. Girlanda, A. Kievsky, and M. Viviani, Phys. Rev. C **84**, 014001 (2011); **102**, 019903(E) (2020).
[29] J. Golak *et al.*, Eur. Phys. J. A **43**, 241 (2010).
[30] K. Hebeler, H. Krebs, E. Epelbaum, J. Golak, and R. Skibiński, Phys. Rev. C **91**, 044001 (2015).
[31] E. Epelbaum *et al.* (LENPIC Collaboration), Phys. Rev. C **99**, 024313 (2019).
[32] P. Reinert, H. Krebs, and E. Epelbaum, Eur. Phys. J. A **54**, 86 (2018).
[33] M. Hoferichter, J. Ruiz de Elvira, B. Kubis, and Ulf.-G. Meißner, Phys. Rev. Lett. **115**, 192301 (2015).
[34] M. Hoferichter, J. Ruiz de Elvira, B. Kubis, and U.-G. Meißner, Phys. Rep. **625**, 1 (2016).
[35] V. G. J. Stoks, R. A. M. Klomp, M. C. M. Rentmeester, and J. J. de Swart, Phys. Rev. C **48**, 792 (1993).
[36] R. N. Pérez, J. E. Amaro, and E. R. Arriola, Phys. Rev. C **88**, 064002 (2013); **91**, 029901(E) (2015).
[37] P. Reinert, H. Krebs, and E. Epelbaum, Phys. Rev. Lett. **126**, 092501 (2021).
[38] E. Epelbaum *et al.*, Eur. Phys. J. A **56**, 92 (2020).
[39] Y. Volkotrub, J. Golak, R. Skibiński, K. Topolnicki, H. Witała, E. Epelbaum, H. Krebs, and P. Reinert, J. Phys. G **47**, 104001 (2020).
[40] V. Urbanevych, R. Skibiński, H. Witała, J. Golak, K. Topolnicki, A. Grassi, E. Epelbaum, and H. Krebs, Phys. Rev. C **103**, 024003 (2021).
[41] A. A. Filin, V. Baru, E. Epelbaum, H. Krebs, D. Möller, and P. Reinert, Phys. Rev. Lett. **124**, 082501 (2020).

[42] A. A. Filin, D. Möller, V. Baru, E. Epelbaum, H. Krebs, and P. Reinert, Phys. Rev. C **103**, 024313 (2021).
[43] K. Hebeler, Phys. Rep. **890**, 1 (2021).
[44] E. Epelbaum, A. Nogga, W. Glöckle, H. Kamada, Ulf.-G. Meißner, and H. Witała, Phys. Rev. C **66**, 064001 (2002).
[45] J. Golak *et al.*, Eur. Phys. J. A **50**, 177 (2014).
[46] H. Witała, J. Golak, R. Skibiński, K. Topolnicki, E. Epelbaum, K. Hebeler, H. Kamada, H. Krebs, U. Meißner, and A. Nogga, Few Body Syst. **57**, 1213 (2016).
[47] K. Sekiguchi *et al.*, Phys. Rev. C **65**, 034003 (2002).
[48] A. Deltuva (private communication, 2018).
[49] W. Glöckle, H. Witała, D. Hüber, H. Kamada, and J. Golak, Phys. Rep. **274**, 107 (1996).
[50] R. J. Furnstahl, N. Klco, D. R. Phillips, and S. Wesolowski, Phys. Rev. C **92**, 024005 (2015).
[51] J. A. Melendez, S. Wesolowski, and R. J. Furnstahl, Phys. Rev. C **96**, 024003 (2017).
[52] E. Epelbaum, PoS **317**, 006 (2020).
[53] K. Schoen, D. L. Jacobson, M. Arif, P. R. Huffman, T. C. Black, W. M. Snow, S. K. Lamoreaux, H. Kaiser, and S. A. Werner, Phys. Rev. C **67**, 044005 (2003).
[54] W. P. Abfalterer, F. B. Bateman, F. S. Dietrich, R. W. Finlay, R. C. Haight, and G. L. Morgan, Phys. Rev. C **63**, 044608 (2001).
[55] K. Ermisch *et al.*, Phys. Rev. C **71**, 064004 (2005).
[56] K. Bodek, J. Golak, L. Jarczyk, S. Kistryn, J. Kuroś-Żołnierczuk, J. Lang, A. Micherdzińska, R. Skibiński, J. Smyrski, M. Sokołowski, J. Sromicki, A. Strzałkowski, H. Witała, J. Zejma, and W. Zipper, Few-Body Syst. **30**, 65 (2001).
[57] M. Allet, K. Bodek, W. Hajdas, J. Lang, R. Müller, S. Navert, O. Naviliat-Cuncic, J. Sromicki, J. Zejma, L. Jarczyk, S. Kistryn, J. Smyrski, A. Strzałkowski, H. Witała, W. Glöckle, J. Golak, D. Hüber, and H. Kamada, Few-Body Syst. **20**, 27 (1996).
[58] R. Skibiński, H. Witała, and J. Golak, Eur. Phys. J. A **30**, 369 (2006).
[59] J. Kuros-Zonierczuk, H. Witała, J. Golak, H. Kamada, A. Nogga, R. Skibiński, and W. Glöckle, Phys. Rev. C **66**, 024003 (2002).
[60] B. S. Pudliner, V. R. Pandharipande, J. Carlson, S. C. Pieper, and R. B. Wiringa, Phys. Rev. C **56**, 1720 (1997).
[61] S. Coon and H. Han, Few Body Syst. **30**, 131 (2001).
[62] A. Nogga, H. Kamada, W. Glöckle, and B. R. Barrett, Phys. Rev. C **65**, 054003 (2002).
[63] A. Nogga, A. Kievsky, H. Kamada, W. Glöckle, L. E. Marcucci, S. Rosati, and M. Viviani, Phys. Rev. C **67**, 034004 (2003).
[64] M. Wang, G. Audi, F. G. Kondev, W. Huang, S. Naimi, and X. Xu, Chin. Phys. C **41**, 030003 (2017).
[65] M. Sanchez Sanchez, N. A. Smirnova, A. M. Shirokov, P. Maris, and J. P. Vary, Phys. Rev. C **102**, 024324 (2020).
[66] Z. T. Lu, P. Mueller, G. W. F. Drake, W. Noertershaeuser, S. C. Pieper, and Z.-C. Yan, Rev. Mod. Phys. **85**, 1383 (2013).
[67] J. L. Friar, J. Martorell, and D. W. L. Sprung, Phys. Rev. A **56**, 4579 (1997).
[68] U. D. Jentschura, A. Matveev, C. G. Parthey, J. Alnis, R. Pohl, T. Udem, N. Kolachevsky, and T. W. Hänsch, Phys. Rev. A **83**, 042505 (2011).
[69] S. Kölling, E. Epelbaum, H. Krebs, and U.-G. Meißner, Phys. Rev. C **80**, 045502 (2009).
[70] S. Kölling, E. Epelbaum, H. Krebs, and U.-G. Meißner, Phys. Rev. C **84**, 054008 (2011).
[71] H. Krebs, E. Epelbaum, and U.-G. Meißner, Few Body Syst. **60**, 31 (2019).
[72] A. Amroun *et al.*, Nucl. Phys. A **579**, 596 (1994).
[73] I. Sick, Phys. Rev. C **90**, 064002 (2014).
[74] I. Sick, Phys. Rev. C **77**, 041302(R) (2008).
[75] E. Tiesinga, P. Mohr, D. Newell, and B. Taylo, The 2018 CODATA Recommended Values of the Fundamental Physical Constants, database developed by J. Baker, M. Douma, and S. Kotochigova, available at http://physics.nist.gov/constants, National Institute of Standards and Technology, Gaithersburg, MD 20899, 2018.
[76] P. A. Zyla *et al.* (Particle Data Group), Prog. Theor. Exp. Phys. **2020**, 083C01 (2020).
[77] H.-W. Hammer and U.-G. Meißner, Sci. Bull. **65**, 257 (2020).
[78] D. Tilley, C. Cheves, J. Godwin, G. Hale, H. Hofmann, J. Kelley, C. Sheu, and H. Weller, Nucl. Phys. A **708**, 3 (2002).
[79] B. R. Barrett, P. Navrátil, and J. P. Vary, Prog. Part. Nucl. Phys. **69**, 131 (2013).
[80] P. Maris, J. P. Vary, and A. M. Shirokov, Phys. Rev. C **79**, 014308 (2009).
[81] S. A. Coon, M. I. Avetian, M. K. G. Kruse, U. van Kolck, P. Maris, and J. P. Vary, Phys. Rev. C **86**, 054002 (2012).
[82] R. J. Furnstahl, G. Hagen, and T. Papenbrock, Phys. Rev. C **86**, 031301(R) (2012).
[83] S. N. More, A. Ekström, R. J. Furnstahl, G. Hagen, and T. Papenbrock, Phys. Rev. C **87**, 044326 (2013).
[84] K. A. Wendt, C. Forssén, T. Papenbrock, and D. Sääf, Phys. Rev. C **91**, 061301(R) (2015).
[85] S. Bogner, R. Furnstahl, P. Maris, R. Perry, A. Schwenk, and J. Vary, Nucl. Phys. A **801**, 21 (2008).
[86] S. Bogner, R. Furnstahl, and A. Schwenk, Prog. Part. Nucl. Phys. **65**, 94 (2010).
[87] R. Roth, A. Calci, J. Langhammer, and S. Binder, Phys. Rev. C **90**, 024325 (2014).
[88] H. M. Aktulga, C. Yang, E. G. Ng, P. Maris, and J. P. Vary, Concurr. Comput.: Pract. Exper. **26**, 2631 (2014).
[89] M. Shao, H. Aktulga, C. Yang, E. G. Ng, P. Maris, and J. P. Vary, Comput. Phys. Commun. **222**, 1 (2018).
[90] P. Maris and J. P. Vary, Int. J. Mod. Phys. E **22**, 1330016 (2013).
[91] E. D. Jurgenson, P. Maris, R. J. Furnstahl, P. Navrátil, W. E. Ormand, and J. P. Vary, Phys. Rev. C **87**, 054312 (2013).
[92] D. Tilley, J. Kelley, J. Godwin, D. Millener, J. Purcell, C. Sheu, and H. Weller, Nucl. Phys. A **745**, 155 (2004).
[93] J. Kelley, J. Purcell, and C. Sheu, Nucl. Phys. A **968**, 71 (2017).
[94] T. Neff, J. Phys. Conf. Ser. **403**, 012028 (2012).
[95] P. Maris, J. Phys. Conf. Ser. **1291**, 012005 (2019).
[96] P. Maris, M. A. Caprio, and J. P. Vary, Phys. Rev. C **91**, 014310 (2015); **99**, 029902(E) (2019).
[97] P. Navrátil, V. G. Gueorguiev, J. P. Vary, W. E. Ormand, and A. Nogga, Phys. Rev. Lett. **99**, 042501 (2007).

[98] T. Dytrych, P. Maris, K. Launey, J. Draayer, J. Vary, D. Langr, E. Saule, M. Caprio, U. Catalyurek, and M. Sosonkina, Comput. Phys. Commun. **207**, 202 (2016).
[99] J. A. Melendez, R. J. Furnstahl, D. R. Phillips, M. T. Pratola, and S. Wesolowski, Phys. Rev. C **100**, 044001 (2019).
[100] C. Drischler, R. J. Furnstahl, J. A. Melendez, and D. R. Phillips, Phys. Rev. Lett. **125**, 202702 (2020).
[101] C. Drischler, J. A. Melendez, R. J. Furnstahl, and D. R. Phillips, Phys. Rev. C **102**, 054315 (2020).
[102] F. Pedregosa, G. Varoquaux, A. Gramfort, V. Michel, B. Thirion, O. Grisel, M. Blondel, P. Prettenhofer, R. Weiss, V. Dubourg, J. Vanderplas, A. Passos, D. Cournapeau, M. Brucher, M. Perrot, and E. Duchesnay, J. Mach. Learn. Res. **12**, 2825 (2011).